

COMPARISON OF LIGO/VIRGO UPPER LIMITS WITH PREDICTED COMPACT BINARY MERGER RATES

KRZYSZTOF BELCZYNSKI¹, SERENA REPETTO², DANIEL E. HOLZ³, RICHARD O'SHAUGHNESSY⁴, TOMASZ BULIK¹, EMANUELE BERTI^{5,6}, CHRISTOPHER FRYER⁷, MICHAL DOMINIK¹,

¹ Astronomical Observatory, Warsaw University, Al. Ujazdowskie 4, 00-478 Warsaw, Poland

² Department of Astrophysics/IMAPP, Radboud University Nijmegen, PO Box 9010, 6500 GL Nijmegen, The Netherlands

³ Enrico Fermi Institute, Department of Physics, and Kavli Institute for Cosmological Physics, University of Chicago, Chicago, IL 60637

⁴ Center for Computational Relativity and Gravitation, Rochester Institute of Technology, Rochester, New York 14623, USA

⁵ Department of Physics and Astronomy, The University of Mississippi, University, MS 38677, USA

⁶ CENTRA, Departamento de Física, Instituto Superior Técnico, Universidade de Lisboa, Avenida Rovisco Pais 1, 1049 Lisboa, Portugal

⁷ CCS-2, MSD409, Los Alamos National Laboratory, Los Alamos, NM 87545

Draft version October 16, 2015

ABSTRACT

We compare evolutionary predictions of double compact object merger rate densities with initial and forthcoming LIGO/Virgo upper limits. We find that: *(i)* Due to the cosmological reach of advanced detectors, current conversion methods of population synthesis predictions into merger rate densities are insufficient. *(ii)* Our optimistic models are a factor of 18 below the initial LIGO/Virgo upper limits for BH-BH systems, indicating that a modest increase in observational sensitivity (by a factor of ~ 2.5) may bring the first detections or first gravitational wave constraints on binary evolution. *(iii)* Stellar-origin massive BH-BH mergers should dominate event rates in advanced LIGO/Virgo and can be detected out to redshift $z \simeq 2$ with templates including inspiral, merger, and ringdown. Normal stars ($< 150 M_{\odot}$) can produce such mergers with total redshifted mass up to $M_{\text{tot},z} \simeq 400 M_{\odot}$. *(iv)* High black hole natal kicks can severely limit the formation of massive BH-BH systems (both in isolated binary and in dynamical dense cluster evolution), and thus would eliminate detection of these systems even at full advanced LIGO/Virgo sensitivity. We find that low and high black hole natal kicks are allowed by current observational electromagnetic constraints. *(v)* The majority of our models yield detections of all types of mergers with advanced detectors. Numerous massive BH-BH merger detections will indicate small (if any) natal kicks for massive BHs. These systems would also shed light on the merger origin, possibly distinguishing mergers arising from field binary evolution (aligned spins) and dense clusters (misaligned spins).

Subject headings: binaries: close — stars: evolution, neutron — gravitation

1. INTRODUCTION

Most massive stars are found in binary systems (e.g., Garcia & Mermilliod 2001; Kiminki et al. 2007; Kobulnicky & Fryer 2007; Sana et al. 2012; Kobulnicky et al. 2014). During the evolution of these stars the binaries can experience component merger during common envelope (CE) phases (e.g., Webbink 1984) or disruption during supernova (SN) explosions (e.g., Tauris & Takens 1998) in which individual stars form neutron stars (NSs) or black holes (BHs). The massive binaries which survive these processes form double compact objects: NS-NS, BH-BH, or mixed BH-NS systems (e.g., Belczynski, Kalogera & Bulik 2002). These remnant systems are subsequently subject to angular momentum loss via the emission of gravitational waves (GWs) and their orbital separation decreases (Peters & Mathews 1963; Weisberg & Taylor 2005). Finally, the two compact objects merge into a single compact object giving rise to a strong GW signal (Einstein 1918).

The LIGO/Virgo network of ground-based interferometric observatories has been designed to search for gravitational-waves, including those resulting from the merger of compact binary systems (Abbott et al. 2009, Accadia et al. 2012)¹. Theoretical predictions for near-future detection probabilities were compiled and presented by Abadie et al. (2010). Initial LIGO/Virgo observations

were concluded in 2010 without the detection of a GW signal (e.g., Abadie et al. 2012). The instruments are currently being upgraded and the network is resuming its operation (2015) and will reach the target sensitivity in a few years (~ 2019).

One of the most promising sources for these advanced GW detectors is the inspiral and merger of NS-NS system. There are several known Galactic double neutron star binaries with merger times shorter than the Hubble time (e.g., Kim, Kalogera & Lorimer 2010). Moreover, observational evidence points to mergers of neutron stars with other neutron stars or black holes as progenitors of short gamma ray bursts (GRBs, Berger, 2013). Recently a first candidate for a kilonova expected to accompany a short GRB if it originates from NS-NS or BH-NS merger has been observed (Berger, Fong & Chornock 2013; Tanvir et al. 2013). Double black hole binaries (BH-BH), on the other hand, remain undetected. Recent theoretical predictions indicate that these systems may either dominate GW observations (e.g., Belczynski et al. 2010a) or be totally absent in the local Universe (e.g., Mennekens & Vanbeveren 2014).

In this study we compare merger rates from our evolutionary calculations of double compact object binaries (Dominik et al. 2012, 2013, 2015) with the latest

¹<http://www.ligo.caltech.edu/>; <http://www.virgo.infn.it/>

LIGO/Virgo upper limits (Abadie et al. 2012; Aasi et al. 2013a, 2014a, 2014b). We also compare our predictions with the expected upper limits of double compact object mergers from advanced GW instruments (Harry et al. 2010; Acernese et al. 2015; Abadie et al. 2015).

2. MERGER RATE DENSITY ESTIMATES

We have employed a set of publicly available evolutionary models from the Synthetic Universe database (<http://www.syntheticuniverse.org>) that provide physical properties and merger rates of NS-NS, BH-NS and BH-BH binaries. The calculations of the mergers were obtained with the **StarTrack** population synthesis code (Belczynski et al. 2002, 2008), with the inclusion of crucial updates in the physical models (winds, common envelope, supernovae). We have chosen several astrophysically motivated models to illustrate the effects of some evolutionary processes on the formation of a NS-NS/BH-NS/BH-BH binaries.

In particular, we explore the effects resulting from common envelope physics and uncertainties in compact object formation (including the supernova mechanism and natal kicks), as well as the effects of metallicity enrichment evolution through cosmic time. Our models use standard initial conditions for population synthesis calculations of massive binaries: thermal distribution of eccentricity ($\propto 2e$), moderate binary fraction (50%), flat in log distribution of orbital separations ($\propto 1/a$), and uniform mass ratio distribution. Recently, Sana et al. (2012) have delivered a set of revised constraints on initial conditions for massive O stars: mostly circular binaries ($\propto e^{-0.42}$), high binary fraction ($> 80\%$), preferentially short orbital periods ($\propto p^{-0.5}$), and uniform mass ratio distribution. However, Kobulnicky & Fryer (2007) and later Kobulnicky et al. (2014) used limits from observations of massive stars and have not found similarly strong constraints; instead, they argue that the orbital parameters are still consistent with the old formulations. Regardless, de Mink & Belczynski (2015) demonstrated that the use of the Sana et al. (2012) initial conditions for massive binaries does not change (within a factor of 2) the double compact object merger rates, and the resulting changes in NS and BH masses are negligible.

Initial LIGO/Virgo have established upper limits on merger rate densities in the local Universe (Abadie et al. 2012; Aasi et al. 2013a). In what follows we make three successively refined estimates for the merger rate density sourced from population synthesis calculations to compare with these existing upper limits and with forthcoming upper limits from the advanced detectors.

2.1. Method I

In the simplest approach one combines high- and low-metallicity models to evaluate Milky Way equivalent galaxy (MWEG) merger rates. Assuming a constant density of MWEGs, the merger rate density may be estimated in the local Universe (Belczynski et al. 2010a).

It is assumed that the local Universe has two components, with a fraction f_Z of local stellar density at solar metallicity ($Z = 0.02$) with an associated Galactic merger rate $\mathcal{R}_{\text{MW}}^{Z_\odot}$, and the remaining $(1 - f_Z)$ of stellar density at low metallicity ($Z = 0.002$) with an associated merger rate

$\mathcal{R}_{\text{MW}}^{0.1Z_\odot}$. We do not use the Asplund et al. (2009) revision of solar metallicity ($Z_\odot = 0.014$). A recent comprehensive analysis of helioseismic and solar neutrino data indicates that this revision is not required (Villante et al. 2014). We use the Galactic merger rates $\mathcal{R}_{\text{MW}}^{Z_\odot}$, $\mathcal{R}_{\text{MW}}^{0.1Z_\odot}$, in units of $[\text{Myr}^{-1}]$, from Dominik et al. (2012). We convert these into merger rate densities in the local Universe via

$$\mathcal{R}_{\text{vol}} = 10^{-6} \rho_{\text{gal}} \left(f_Z \mathcal{R}_{\text{MW}}^{Z_\odot} + (1 - f_Z) \mathcal{R}_{\text{MW}}^{0.1Z_\odot} \right) \text{Mpc}^{-3} \text{yr}^{-1}, \quad (1)$$

where we take the local density of Milky Way-like galaxies to be $\rho_{\text{gal}} = 0.0116 \text{Mpc}^{-3}$ (e.g., Kopparapu et al. 2008). In this calculation a constant star formation rate was assumed for MWEGs at a level of $3.5 \text{M}_\odot \text{yr}^{-1}$ for a duration of 10 Gyr (this results in approximately the mass found in stars in the present day Milky Way). Only double compact objects that are formed with delay times (time elapsed from their formation on the Zero Age Main Sequence to their merger) shorter than 10 Gyr (the age of the Galactic disk) contribute to the merger rate density.

The investigation of $\sim 30,000$ Sloan Digital Sky Survey galaxies revealed that recent (within the last ~ 1 Gyr) star formation was bimodal, with about half of the stars formed with high metallicity, and the other half with low metallicity (Panter et al. 2008). We thus use a 50%-50% combination of two stellar populations, one with high and one with low metallicity ($f_Z = 0.5$).

Note that this method mostly ignores the star formation rate (SFR) evolution through cosmic time. It assumes a constant star formation rate per MWEG, so there is no merger density variation as a function of distance/redshift, and it uses a very crude approximation of metallicity evolution over the history of the Universe, characterized by only two discrete metallicities. We also ignore selection effects in the GW detection of the binaries, such as accounting for how a given detector's reach depends upon binary merger mass.

2.2. Method II

The second method takes into account the star formation history and metallicity evolution through cosmic time. It also incorporates the full gravitational radiation waveforms and detector sensitivity noise curves. This method utilizes groundwork and models developed in Dominik et al. (2013, 2015).

The calculation begins with a SFR model across cosmic time (the Madau plot; e.g., Madau & Dickinson 2014) and metallicity evolution models. The metallicity evolution is only weakly constrained, especially for large redshifts, and therefore Dominik et al. (2013) have employed two models differing by the fraction of low-metallicity stars as a function of redshift. At each redshift there is a spread of metallicity of the stars formed in each model. The rate at which the average metallicity increases with cosmic time is constant in both models. At redshift $z = 0$ the low-metallicity model results in a median metallicity of $0.8 Z_\odot$, while for the high-metallicity model the median is at $1.5 Z_\odot$. In a nutshell, at any given time (or redshift) the average metallicity of star forming gas differs by a factor of ~ 2 between the two models.

Population II and Population I stars are evolved with population synthesis over a large redshift range ($z = 0-$

20) and metallicity range ($Z = 0.0001\text{--}0.03$). Double compact objects are formed and propagated in time to their merger point. As a result we obtain self-consistent merger rate densities as a function of redshift for NS-NS, BH-NS and BH-BH binaries (see Figs. 3 and 5 of Dominik et al. 2013 or <http://www.syntheticuniverse.org>). In what follows we present a method to evaluate which mergers are within the volume sampled by a GW detector of a given sensitivity.

We assume that a given event is “detected” when it satisfies our detectability criterion: the source surpasses a signal-to-noise ratio (SNR) threshold in a single GW detector:

$$\text{SNR} > 8.0. \quad (2)$$

This single detector criterion approximately translates into $\text{SNR} > 12$ for a 3-detector network (e.g., two LIGO and one Virgo detectors). This is conventionally used as the threshold for a GW detector network to be able to identify the GW signal from a merging binary (e.g., Abadie et al. 2010).

For the initial LIGO/Virgo observations we use a simple analytical approximation to the noise power spectral density given in eq. 3.1 of Ajith & Bose (2009; see also Tab. I of Sathyaprakash & Schutz 2009). For advanced LIGO/Virgo we adopt a noise model from an analytical approximation to the advanced LIGO zero-detuning high power noise power density of Ajith (2011; see their eq. 4.7). This approximation allows for effective observations above ~ 20 Hz and is in excellent agreement with the official advanced LIGO design noise curve (Shoemaker et al. 2010).

Initial and advanced LIGO/Virgo rate estimates are obtained using gravitational waveform models for a given source with binary component masses m_1 and m_2 at redshift z . Our standard waveform model IMRPhenomC from Santamaria et al. (2010) includes inspiral, merger, and ringdown, and is tuned to numerical relativity simulations of non-precessing BH-BH mergers with aligned spins. We have verified explicitly that we obtain essentially identical rate estimates using an effective-one-body waveform model (more specifically, EOBNRv2; Pan et al. 2011). Mild differences between EOBNRv2 and IMRPhenomC only show up in the highest mass bins, where the rates are so low that statistical fluctuations dominate over uncertainties due to the gravitational waveform model. Panarale et al. (2013) demonstrated that finite-size effects introduce negligible errors ($\lesssim 1\%$) in SNR calculations for BH-NS binaries, and therefore the IMRPhenomC model is also applicable to BH-NS rate estimates. We also use the IMRPhenomC waveforms for NS-NS binaries, since in this case the signal seen by advanced detectors is dominated by the early inspiral, where finite-size effects are negligible. The IMRPhenomC model includes higher harmonics in the waveform amplitude, resulting in a slight reduction of the inspiral amplitude compared to a simple quadrupole-formula estimate, and therefore in a slight decrease in the predicted detection rates. All of our rate calculations neglect spins, and therefore they should be considered as conservative lower limits (cf. Dominik et al. 2015 for a more detailed discussion of waveform models and of the effect of spins).

The detectability criterion of eq. 2 was applied to all population synthesis models in Dominik et al. (2013).

Mergers satisfying this criterion were selected and can be found online at <http://www.syntheticuniverse.org> following the link to “Double Compact Objects” and then the link to “Upper Limits”. In particular, these files include a list of merger events that are potentially detectable (i.e., are within the horizon redshift) of the initial and advanced LIGO/Virgo detectors. For each merger we list the intrinsic source-frame component masses (m_1 and m_2), the redshift of the merger (z), the SNR value for this binary assuming it is *optimally located and oriented*, the horizon redshift for this binary (z_{hor}), and the merger rate density associated with a given event in the rest frame of the merger (s). This merger rate density is expressed in comoving volume units and refers to time as measured by a clock at the merger; it has units of $\text{Mpc}^{-3}\text{yr}^{-1}$. The horizon redshift indicates the redshift at which a particular binary merger with redshifted mass: $m_1(1+z_{\text{hor}})$ and $m_2(1+z_{\text{hor}})$ would have $\text{SNR} = 8.0$ if it were optimally located and oriented with respect to a given detector. We then follow the method described below to calculate the merger rate density within the volume sampled by a GW detector of a given sensitivity.

We adopt a standard flat cosmology with $H_0 = 70.0 \text{ km s}^{-1} \text{ Mpc}^{-1}$, $\Omega_m = 0.3$, and $\Omega_\Lambda = 0.7$ (and thus $\Omega_k = 0$). The following relations, adopted from Hogg (2000), are used in our estimates. We present them explicitly for definiteness and to establish our notation. The relationship between redshift and (lookback) time is given by

$$t(z) = t_H \int_z^\infty \frac{dz'}{(1+z')E(z')}, \quad (3)$$

where $t_H = 1/H_0 = 13.969$ Gyr is the Hubble time, and $E(z) = \sqrt{\Omega_M(1+z)^3 + \Omega_k(1+z)^2 + \Omega_\Lambda}$. The resulting age of the Universe is $t(0) = 13.47$ Gyr. The comoving volume element dV_c/dz is given by

$$\frac{dV_c}{dz}(z) = \frac{c}{H_0} \frac{D_c^2}{E(z)}, \quad (4)$$

where c is the speed of light in vacuum, and where the comoving distance D_c is given by

$$D_c(z) = \frac{c}{H_0} \int_0^z \frac{dz'}{E(z')}. \quad (5)$$

From the comoving distance we can easily compute the luminosity distance (D_l) for our adopted model of cosmology (with $\Omega_k = 0$):

$$D_l = (1+z)D_c. \quad (6)$$

Every merger from our population synthesis simulation is a proxy for a certain merger rate density:

$$s_i = \frac{d\text{SFR}}{dZ} \Delta Z \frac{1}{M_{\text{sim}}}, \quad (7)$$

where $\frac{d\text{SFR}}{dZ} \Delta Z$ is the fractional star formation rate in the simulated metallicity interval, and M_{sim} is the total mass of single and binary stars (within our adopted initial mass function range: $0.08\text{--}150 M_\odot$) in the simulation. If a given merger from the population synthesis model satisfies eq. 2, then the merger rate density which it represents, s_i , contributes to the total merger rate density. The contribution

to the merger rate (in the observer frame) associated with one particular simulated merger i is

$$r_i = 4\pi p_{\text{det}} \left(\frac{8.0}{\text{SNR}} \right) s_i \frac{1}{1+z} \frac{dV_c}{dz} \frac{dz}{dt} \Delta t \text{ yr}^{-1}, \quad (8)$$

where the factor $1/(1+z)$ transfers the merger rate density s_i from the rest frame to the observer frame, the factor dV_c/dz is the comoving volume element, the factor $(dz/dt)\Delta t$ allows us to integrate in time rather than redshift, and the factor of 4π takes into account the entire sky (i.e., integration over the solid angle). The population synthesis predictions were performed in finite time bins of $\Delta t = 100$ Myr. Both dz/dt (eq. 3) and dV_c/dz (eq. 4) are evaluated at the merger redshift. Finally, $p_{\text{det}}(w)$ is a detection probability (with value in the range 0–1) that takes into account the detector antenna pattern. This factor translates from s_i – which represents the density within the entire spherical volume enclosed by the horizon redshift – to the merger rate density within the “peanut-shaped” volume sampled by the detectors. To calculate this factor we use the approximation from the Appendix of Dominik et al. (2015):

$$p_{\text{det}}(w) = a_2(1-w/\alpha)^2 + a_4(1-w/\alpha)^4 + a_8(1-w/\alpha)^8 + (1-a_2-a_4-a_8)(1-w/\alpha)^{10}, \quad (9)$$

where $a_2 = 0.374222$, $a_4 = 2.04216$, $a_8 = -2.63948$ and $\alpha = 1.0$. Each r_i is the contribution to the merger rate from a particular event i , and by summing over all such contributions our estimate takes into account the antenna pattern of the GW detectors.

We calculate merger rate densities within a set of redshifted total merger mass bins. Each bin includes some number of events (n), where each event is associated with its own specific merger mass and merger redshift. GW detectors do not provide measurements of the intrinsic merger masses, but instead are sensitive to the redshifted merger masses². A merger is described (and assigned to a given mass bin) by its redshifted mass, as measured at the detector. The total redshifted mass of a binary merging at redshift z , as observed today ($z = 0$), is defined by

$$M_{\text{tot},z} = (m_1 + m_2)(1+z), \quad (10)$$

where $M_{\text{tot},i} = (m_1 + m_2)$ is the intrinsic total mass of a given merger. These cosmological factors will become increasingly important as advanced detectors begin to probe the Universe to significant redshifts (up to $z \sim 2$ for heavy BH-BH mergers), implying that the most distant binaries are less massive than they appear to be in our detectors. Our results could easily be translated into chirp (M_{chirp}) and redshifted chirp mass ($M_{\text{chirp},z}$):

$$M_{\text{chirp},z} = M_{\text{chirp}}(1+z) = \frac{(m_1 m_2)^{3/5}}{(m_1 + m_2)^{1/5}}(1+z). \quad (11)$$

The total merger rate for a given redshifted mass bin within the volume sampled by a given detector is then calculated from

$$r_{\text{tot}} = \sum_{i=1}^n r_i \text{ yr}^{-1}. \quad (12)$$

²It may be possible to infer a redshift distribution from the distance posteriors of a given event, and thereby infer a distribution over intrinsic merger mass. This is unlikely to be a productive exercise until significant numbers of detections arise, and statistical analyses can be performed.

The n events are generated, via population synthesis, from the entire cosmic star formation history (Population I and II; Population III is not included as discussed in Dominik et al. 2013). Note that summing up merger rates from a range of redshifts, as we have done above, results in the loss of information about the redshift dependence of the merger rate. Note also that both r_i and r_{tot} are *detection* rates.

The total merger rate density for a given redshifted total mass bin within the peanut-shaped comoving volume sampled by a given detector may be calculated from

$$\mathcal{R}_{\text{tot}} = \frac{r_{\text{tot}}}{V_{\text{antenna}}} \text{ Mpc}^{-3} \text{ yr}^{-1}, \quad (13)$$

where V_{antenna} indicates the comoving volume within a peanut-shaped (antenna) volume for the given mass bin. It is to be noted that this comoving volume is different for mergers with different mass, and so the effective total volume represented by a population is defined by a weighted sum over all the binaries:

$$V_{\text{antenna}} = \sum_{i=1}^n \frac{r_i}{r_{\text{tot}}} V_{\text{antenna},i}. \quad (14)$$

For a given merger with component masses m_1 and m_2 and the corresponding horizon redshift $z_{\text{hor},i}$, we estimate the comoving volume from:

$$V_{\text{antenna},i} = 4\pi \int_0^{z_{\text{hor}}} \frac{1}{1+z} \frac{dV_c}{dz} p_{\text{det}} \left(\frac{D_1(z)}{D_1(z_{\text{hor}})} \right) dz \text{ Mpc}^3, \quad (15)$$

where all factors appearing in the integral were defined earlier in this section.

Note that previous estimates (e.g., method I) neglect the fact that the merger rate density may change with redshift. In particular, for many models the merger rate density increases with increasing redshift (e.g., see Dominik et al. 2013; Figs. 3 and 5). This increase may be quite significant (factor of $\gtrsim 10$) within the volume sampled by advanced GW detectors (the most massive BH-BH mergers can be seen from as far as redshift of $z = 2$; see Sec. 2.4 and 5.2). Therefore, the use of a constant merger rate density at any given redshift (e.g., $z = 0$) is a major oversimplification. Estimates of the merger rate density must be integrated over the volume sampled by a specific detector for all sources.

There are two crucial factors in the evaluation of merger rates or merger rate densities from modern population synthesis calculations that take into account SFR and metallicity evolution with redshift: a proper accounting of cosmology, and the inclusion of population synthesis results out to the horizon (and not just the range) of the detectors. We now elaborate on these two points in turn.

First, the effective volume included in the peanut-shaped antenna pattern sampled by a GW detector *cannot* be reliably calculated with simple formulas that utilize the Euclidean approximation. For example, initial

LIGO/Virgo estimates typically used the so-called range distance and volume:

$$D_{\text{range}} = \frac{D_{\text{hor}}}{2.264}, \quad (16)$$

$$V_{\text{range}} = \frac{V_{\text{hor}}}{(2.264)^3} = \frac{V_{\text{hor}}}{11.605}, \quad (17)$$

where $\omega = 2.264$ is the reduction factor that takes into account random sky positions and source orientations (i.e., “sky and inclination averaged”), D_{hor} is the luminosity distance corresponding to the horizon redshift, and V_{hor} is the entire (spherical) volume enclosed within the horizon redshift. For example, the volume within the horizon redshift $z_{\text{hor}} = 2$ (relevant for advanced detectors; see Sec. 5.2) is $V_{\text{hor}} = 58.0 \times 10^{10} \text{ Mpc}^3$ (integral of eq. 4). This leads to a range volume of $V_{\text{range}} = 5.0 \times 10^{10} \text{ Mpc}^3$ using eq. 17, and to a much larger value of $V_{\text{range}} = 16.2 \times 10^{10} \text{ Mpc}^3$ using eq. 16 (where D_{range} is used to calculate the range redshift z_{range} via eq. 6, and this in turn is used to calculate the range volume from the integral of eq. 4). Taking into account cosmology, the correct expression is eq. 15, which produces a volume of $V_{\text{antenna}} = 7.1 \times 10^{10} \text{ Mpc}^3$.

Second, when using population synthesis results which produce merger rates that vary with redshift, it is necessary to account for all sources (alas with diminishing probability defined by p_{det}) all the way out to the horizon redshift; the inclusion of events only out to the range redshift is insufficient. Redshift evolution of merger rates is fully expected: these rates are predicted to change by a factor of ~ 10 in the redshift range $z = 0-2$ (Dominik et al. 2013).

In what follows we abstain from the use of the term “range” in our calculations and text, and the term “antenna” to denote the volume sampled by a given (initial or advanced) detector.

Our method utilizes the astrophysical knowledge of the sources (single and binary evolution in population synthesis models) combined with the cosmological evolution of the SFR and metallicity, while also incorporating the full waveforms (inspiral-merger-ringdown) from the merging sources and the detailed detector noise curves. There are of course many uncertainties, some very important, in the underlying evolutionary models. Furthermore, there are minor uncertainties introduced by unknowns associated with the cosmological parameters, the waveforms, and the future noise curves of the advanced LIGO detectors. Although specific parts of our analysis may be updated in the future with improved and revised input physics, our basic framework for calculating the merger rate density within a cosmological context should remain applicable.

There is one potential issue that should be taken into account while working with GW observations (whether these are upper limits or detections). Observational imperfections or statistical GW measurement errors (due to noise fluctuations) will affect any comparison with theoretical models. This issue may be addressed in two different ways: corrections may be applied to the population synthesis model predictions, or the GW detection errors may be incorporated into observations and presented as uncertainties on the measured upper limits/detection rates. The practical application of the former approach is presented in Stevenson, Ohme, & Fairhurst (2015), while here we

adopt the latter approach and assume that the observational uncertainties are appropriately accounted for.

2.3. Method III

In method III we compute merger rate densities based on the *entire* spherical volume enclosed by the horizon redshift, and not just within the peanut-shaped detector antenna pattern as was pursued in method II. In the following we only rewrite those equations which are modified with respect to method II (see Sec. 2.2).

The observer frame merger rate associated with one particular event i is:

$$r_i = 4\pi s_i \frac{1}{1+z} \frac{dV_c}{dz} \frac{dz}{dt} \Delta t \text{ yr}^{-1}, \quad (18)$$

where all the factors have already been introduced in Sec. 2.2. This is the contribution to the merger rate from a particular event i , and we will sum all these contributions all the way to the horizon distance for each observed mass bin. Note that the detection probability factor p_{det} does not appear in eq. 18.

The total merger rate density for a given redshifted total mass bin within spherical comoving volume limited by the horizon redshift is given by

$$\mathcal{R}_{\text{tot}} = \frac{r_{\text{tot}}}{V_{\text{hor}}} \text{ Mpc}^{-3} \text{ yr}^{-1}, \quad (19)$$

where V_{hor} indicates the comoving volume within the horizon redshift z_{hor} for a given redshifted total mass bin. This quantity is estimated by integrating eq. 4:

$$V_{\text{hor}} = \frac{4\pi}{3} D_c^3(z_{\text{hor}}), \quad (20)$$

where D_c is given by eq. 5.

If the merger rate density were constant (from the point of view of the observer frame, so constant in redshifted mass and redshifted time bins) out to the horizon redshift, z_{hor} , then the inferred rate densities within the peanut (method II) and within the full volume (method III) would be identical. However, it would be a very striking coincidence if the merger rate density of double compact objects is constant out well beyond the Hubble flow. Double compact object formation depends on the star formation rate and on various properties of the stars that form compact objects (e.g., metallicity, binarity, IMF). It is well established that at least some of these quantities/properties change with redshift (e.g., SFR and metallicity), and therefore it seems highly unlikely that these redshift dependent factors result in a constant merger rate density in the observer frame. The relevant question for our study is: how significantly does the merger rate density change when going from $z = 0$ to the horizon redshift?

A first intuitive estimate can be easily arrived at: if coalescence times for double compact objects are short, then the merger rate density will evolve with redshift in a similar fashion to the SFR. Within the horizon redshift for the most massive BH-BH mergers ($z_{\text{hor}} = 2$), the SFR increases by a factor of ~ 10 , implying a similarly dramatic evolution in merger rate. This intuitive expectation (modified somewhat by other factors, such as metallicity evolution with redshift) is confirmed by detailed population synthesis estimates (Dominik et al. 2013).

LIGO/Virgo will sample merger rate densities (although with decreasing sensitivity) all the way out to the horizon

redshift. In principle, knowing the antenna pattern and assuming a prior on the merger rate density redshift dependence, it is possible to infer from the number of observed binaries an estimate of the upper limit or merger rate density in the entire spherical volume enclosed within the horizon redshift. Moreover, in the case when there are plentiful detections, the rate can be estimated observationally for specific distance (or redshift) intervals.

2.4. Comparison of Methods

In what follows we present the merger rate density divided into bins of redshifted total merger mass. Since GW detectors will measure the redshifted mass of mergers, we therefore use the redshifted total merger mass from our simulations (eq. 10). The specific limits on the bins are adopted from the initial LIGO/Virgo upper limits papers for low- and high-mass inspirals (Abadie et al. 2012; Aasi et al. 2013a), with a highest mass bin consisting of 91–109 M_{\odot} . We extend this binning, with bin width of 18 M_{\odot} , out to a maximum of 500 M_{\odot} . This choice is arbitrary, and can be changed if desired.

In Figure 1 and Table 1 we present the dependence of the merger rate density on the calculational method (method I, II, and III). For this exercise we have used one specific population synthesis model, so as to highlight the differences in our merger rate density calculations. In methods II and III we employ the evolutionary model V2 with low metallicity enrichment; this model utilizes restricted CE survival (see Sec. 3). In method I we use the same evolutionary model V2, but the metallicity evolution treatment is oversimplified. Additionally, in this case no merger redshift information is available, so only the intrinsic total merger masses are used. Obviously, if we assume – as we have – a constant comoving density of Milky Way-like galaxies (see eq. 1), we can draw from a random distribution of redshifts. However this modification is not applied to our calculations, as our intent is to emphasize the differences between the methods that use (or do not use) redshift information about the mergers. For a comparison we also include the expected advanced LIGO/Virgo upper limits (see Sec. 4.2). We find strikingly large differences between method I and the other two methods of merger rate density calculation.

Methods II and III generate very similar merger rate densities for relatively low mass mergers ($M_{\text{tot},z} < 70 M_{\odot}$). For higher total redshifted merger masses, method III predicts consistently higher merger rate densities than method II. This is expected, as by construction method III samples a larger high-redshift volume than method II. The BH-BH merger rate density increases with redshift within the entire advanced LIGO/Virgo horizon of about $z_{\text{hor}} = 2$ (see Sec. 2.4 and 5.2).

Methods II and III predict nonzero rates out to a total redshifted mass of 400 M_{\odot} . This is a much higher total BH-BH binary mass than what is conventionally expected from normal stars, where by “normal” stars we mean stars with initial mass below 150 M_{\odot} . Until recently, this value was believed to be the upper mass limit on star formation, at least in non-zero metallicity environments. Thus far all the predictions for compact object merger rates from Population I and Population II stars have been limited to stars of mass $< 150 M_{\odot}$. The recent discovery of stars estimated to be initially as massive as $\sim 200\text{--}300 M_{\odot}$

(e.g., Crowther et al. 2010) in the relatively high metallicity environment of the S Doradus cluster in the LMC ($Z \approx 0.6 Z_{\odot}$) has shaken these beliefs. The first study of BH-BH merger rates from these very massive stars has already been proposed (Belczynski et al. 2014). However, in the current work our models are limited to stars with initial mass below 150 M_{\odot} and we nonetheless find mergers as massive as 400 M_{\odot} in our calculations. Two factors are responsible for this surprising result: the inclusion of very low-metallicity models, and our use of the full gravitational waveform in our analysis. The former allows for the formation of massive BH-BH binaries from Population II stars even if these are limited to 150 M_{\odot} , while the latter allows for the detection of high mass BH-BH mergers from large distances, thereby redshifting the intrinsic total merger mass to higher values (see eq. 10).

For the evolutionary models we use in this study, the most massive BH-BH binary is formed at our lowest adopted metallicity ($Z = 0.0001$) from two stars with very high initial (Zero Age Main Sequence) mass: $m_{\text{zams},1} = 148 M_{\odot}$ and $m_{\text{zams},2} = 144 M_{\odot}$. The detailed evolutionary sequence is described in Dominik et al. (2013; see their Sec. 5.1) and it ends in the formation of a BH-BH binary with a total intrinsic BH-BH mass of $M_{\text{tot},i} = 136 M_{\odot}$ (component masses of 74 M_{\odot} and 62 M_{\odot}). This is not surprising within the adopted evolutionary framework, as wind mass loss is ineffective at such low metallicity *and* the most massive BHs form via direct collapse without a supernova event (and its associated mass loss). This highlights the physically motivated possibility of such high mass scenarios, given our assumptions. Our application of the full waveform for such a merger allows us to state that the merger, with a redshifted mass of $M_{\text{tot},z} \simeq 408 M_{\odot}$, remains detectable with the advanced LIGO detectors out to a redshift of $z = 2$. Such high redshifts are not generally considered accessible in the context of GW observations with second generation instruments, but if these sources exist they may be potentially detected at these vast distances. Our evolutionary predictions place such high mass ($\sim 400 M_{\odot}$) events at very low merger rate density; $\sim 5\text{--}8$ orders of magnitude below forecasted advanced LIGO/Virgo upper limits. However, at somewhat smaller total redshifted merger mass ($\sim 300\text{--}350 M_{\odot}$) the predictions are only $\sim 1\text{--}3$ orders of magnitude below upper limits making detections feasible. This is especially true if we consider 10 years of advanced LIGO/Virgo observations. Note also that such massive mergers could result from other formation mechanisms (Belczynski et al. 2014).

The merger rate densities predicted with method I are very different from those obtained from the more physical and self-consistent approaches in methods II and III. The only agreement is found for NS-NS binaries, for which all three methods agree. However, for BH-NS and BH-BH binaries there is striking disagreement: for low mass binaries ($5\text{--}35 M_{\odot}$) method I produces a merger rate density that is $\sim 5\text{--}10$ times higher than from method II or III, and for higher mass binaries the method I merger rate density quickly drops below the rates from method II and III.

Method I does not produce any mergers with total intrinsic mass above 50 M_{\odot} , while methods II and III allow for non-zero merger rate densities of systems with total

observed mass up to $400 M_{\odot}$. Note that these striking differences are obtained with the same underlying evolutionary model and therefore can be fully associated to (1) the differences in calculation methods, (2) the much broader range of metallicity in methods II and III ($Z = 0.0001$ – 0.03) as compared to method I ($Z = 0.002$ – 0.02), and (3) the fact that there is no redshift information available in method I, so the merger mass is not redshifted. However, even if we apply a redshift to the total mass of *all* the mergers in method I using *the most extreme* redshift of potentially detectable binaries ($z = 2$), the maximum redshifted mass in our suite of simulations from method I would still only reach $150 M_{\odot}$.

The remaining part of the difference comes from the fact that method I uses only two metallicities ($Z = 0.002$ and $Z = 0.02$) while methods II and III incorporate a much broader spectrum of metallicity (11 values spanning the range $Z = 0.0001$ – 0.03). Metallicity is a very important factor in the formation of BH-BH mergers (Belczynski et al. 2010a). In a nutshell, decreasing metallicity decreases wind mass loss and can increase the chance of common envelope development/survival, thereby enhancing the formation of close and massive BH-BH binaries. As a result, the maximum intrinsic total mass of a BH-BH binary is $M_{\text{tot},i} = 42 M_{\odot}$ ($24 + 18 M_{\odot}$ system formed at metallicity $Z = 0.002$) using method I, and $M_{\text{tot},i} = 136 M_{\odot}$ ($74 + 62 M_{\odot}$ system formed at $Z = 0.0001$) using methods II or III. The specific double compact object formation channels and the mass dependence of double compact objects on metallicity is discussed by Dominik et al. (2012; 2013).

The above discussion argues against using simple methods, such as method I, to make comparisons with advanced GW observations. Note that merger and detection rate estimates for double compact objects (many of which come from past studies with the *StarTrack* population synthesis code; e.g., Belczynski et al. 2002) collected in Abadie et al. (2010) use only a *single* value of metallicity ($Z = 0.02$). It is important to note that this value strongly disfavors the formation of BH-BH mergers. Since metallicity can significantly alter the predicted rates, and since merger rate estimates must be framed in a cosmological context in the advanced detector era, the Abadie et al. (2010) estimates for the stellar-origin double compact object merger rates must be significantly updated.

In summary, we find that method I is significantly flawed, especially at higher mass, and we do not use it in what follows. We will use method II for *all* of our comparisons with the initial and advanced LIGO/Virgo upper limits.

3. EVOLUTIONARY MODELS

Following Dominik et al. (2013; 2015) we consider four evolutionary models (see Table 2 for model summaries). The models employ the current best estimates for various physical parameters, including some that are not yet fully constrained but play an important role in the formation of double compact objects. For example, during CE evolution physical estimates of the donor envelope binding energy are used (Xu & Li 2010; as revised by Dominik et al. 2012), we adopt $M_{\text{NS,max}} = 2.5 M_{\odot}$ as the maximum NS mass (Lattimer & Prakash 2011), we assume the

NS natal kick distribution, based on observations to be a Maxwellian with $\sigma = 265 \text{ km s}^{-1}$ (Hobbs et al. 2005), BH natal kicks are smaller and due to a mass ejection mechanism (Fryer et al. 2012), the compact object mass spectrum is based on rapid supernova explosions (Belczynski et al. 2012), the stellar winds are revised for the effects of clumping (Vink, de Koter & Lamers 2001) and constrained by black hole mass estimates (Belczynski et al. 2010b), and we adopt non-conservative mass transfer episodes with 50% of the mass retained in the binaries (Meurs & van den Heuvel 1989).

In models V1 and V2 we test the potential suppression of the NS-NS/BH-NS/BH-BH formation in case B Roche lobe overflow (RLOF). If the RLOF proceeds on the dynamical timescale of the donor star a given binary evolves through a common envelope (CE) phase. The severe orbital decay during CE is one of the mandatory conditions in the formation of close double compact objects. However, it is not at all clear whether massive Hertzsprung gap (HG) donors (case B) have clear core-envelope structure (Belczynski et al. 2007) and whether they behave like MS stars (always resulting in a CE merger) or evolved giant stars (with potential CE survival). Additionally, the conditions for CE development are not fully understood (e.g., Ivanova et al. 2013). This is true in particular for massive stars that may have radiative envelopes during most of their HG life and may potentially evolve through thermal timescale RLOF rather than CE. Such evolution would not provide any significant binary orbit contraction, and it would result in wide NS-NS/BH-NS/BH-BH formation. Conditions for CE development are critical in the formation of close (merging) double compact objects, and are currently under study with the detailed evolutionary code MESA (Pavlovski, Belczynski, & Ivanova, in preparation). In model V1 we adopt an optimistic scenario and allow HG stars to survive through the CE phase. In model V2 we remove from our simulations all potential NS-NS/BH-NS/BH-BH progenitors that encounter CE with an HG donor star; this is probably more physically realistic than model V1. We use model V2 as our standard (reference) model, and we use its relevant CE physics in subsequent models.

In models V3 and V4 we test supernova/core-collapse physics. In particular in model V3 we adopt high BH natal kicks (drawn from a 1-D Maxwellian with $\sigma = 265 \text{ km s}^{-1}$). Such high kicks are most often adopted for NSs. In all other models the BH natal kicks are much smaller and we describe these particular choices in more detail in Sec. 6.9. In model V4 we change the underlying supernova/core-collapse model, and the resulting NS/BH mass spectrum changes from one with a mass gap (models V1,V2 and V3) to a continuous spectrum without a gap. The mass gap (lack of compact objects in mass range 2 – $5 M_{\odot}$) has been a puzzling observation for over a decade (Bailyn 1998). At present the origin of the gap remains unclear. It has been proposed that the gap is just an observational artifact (Kreidberg et al. 2012). Alternatively, the gap may be set by the very short time in the development of a supernova explosion in the neutrino supported convective engine model (Belczynski et al. 2012).

For all models we use a typical Initial Mass Function (IMF) with slope of -2.7 for massive stars, 50% binary

fraction, thermal distribution for initial eccentricity, and flat in logarithm initial distribution of initial separations (as described in detail in Dominik et al. 2012). We have assumed that the IMF ends at $150 M_{\odot}$. As discussed above, this may no longer be true given the massive stars discovered in the R136 cluster in the LMC (Crowther et al. 2010). We have dedicated a separate study to investigate the formation of BH-BH binaries from such very massive stars (Belczynski et al. 2014). The initial distributions may also appear outdated; new measurements of O-type stars indicated quite different distributions for orbital periods and eccentricities (Sana et al. 2012). However, adopting the new distributions does not significantly affect the merger rates nor the masses of double compact object (de Mink & Belczynski 2015).

4. OBSERVATIONS

4.1. Initial LIGO/Virgo upper limits

The LIGO/Virgo S6 run (completed in 2010) combined with earlier searches (initial LIGO/Virgo) was used to derive upper limits on double compact object merger rate densities. For mergers with total mass below $25 M_{\odot}$ the upper limits were provided in seven mass bins: $2\text{--}5 M_{\odot}$, $5\text{--}8 M_{\odot}$, $8\text{--}11 M_{\odot}$, $11\text{--}14 M_{\odot}$, $14\text{--}17 M_{\odot}$, $17\text{--}20 M_{\odot}$, $20\text{--}25 M_{\odot}$ (Abadie et al. 2012; see their Fig. 4). This search was performed utilizing only the inspiral part of the waveform templates adequate for low mass mergers.

For mergers with higher total mass the upper limits were provided as a function of the two component masses (Aasi et al. 2013a; see their Fig. 5 and Table 1). These upper limits were obtained with full waveforms including inspiral, merger and ringdown. The deepest upper limits correspond to equal mass binaries. For example, the upper limit for a detection of a $50\text{--}50 M_{\odot}$ BH-BH merger is $0.7 \times 10^{-11} \text{ Mpc}^{-3} \text{ yr}^{-1}$, which is a factor of ~ 5 lower than the $3.8 \times 10^{-11} \text{ Mpc}^{-3} \text{ yr}^{-1}$ limit for the $77\text{--}23 M_{\odot}$ merger. This is the most extreme case of upper limit difference for the same total mass but different mass ratio presented in Aasi et al. (2013a). Typically, the change from equal mass binary to uneven mass binary results in increasing upper limits by less than a factor of 2. For example, the upper limit changes from $3.3 \times 10^{-11} \text{ Mpc}^{-3} \text{ yr}^{-1}$ for a $23\text{--}23 M_{\odot}$ merger to $4.2 \times 10^{-11} \text{ Mpc}^{-3} \text{ yr}^{-1}$ for a $32\text{--}14 M_{\odot}$ merger (change of only ~ 1.3).

The adoption of equal mass upper limits provides the most optimistic estimates and the closest approach with evolutionary model predictions for the merger rate density. Keeping this in mind, we note that our recent evolutionary predictions typically generate BH-BH binaries with comparable mass components (average mass ratio of 0.8; see Fig. 9 of Dominik et al. 2012). On the other hand, BH-NS binaries are predicted to form with extreme mass ratios (average mass ratio of 0.2; also see Fig. 9 of Dominik et al. 2012). However, it is not expected that their total mass would typically exceed $25 M_{\odot}$. If this is the case, then most BH-NS mergers would contribute in bins covered by the low mass search, in which a uniform distribution of primary mass was adopted (Abadie et al. 2012). This makes these upper limits applicable to BH-NS mergers.

Technically, the borders of high mass bins adopted in our study were obtained from mid points between five equal mass binaries presented by Aasi et al. (2013a) along with

the quoted S5+S6-Vsr2/3 EOBNR upper limits. For example, the first two equal mass binaries in Table 1 of Aasi et al. (2013a) are $14\text{--}14 M_{\odot}$ ($M_{\text{tot}} = 28 M_{\odot}$) and $23\text{--}23 M_{\odot}$ ($M_{\text{tot}} = 46 M_{\odot}$) with the mid point in total mass of $37 M_{\odot}$. That gives us the first high mass bin: $25 M_{\odot}$ (the end point of low mass search binning) to $37 M_{\odot}$ (the mid point between the first two equal mass binaries in high mass search).

4.2. Advanced LIGO/Virgo upper limits

We have calculated the expected upper limits for the design advanced LIGO/Virgo sensitivity. As discussed near Eq. 2, we conservatively assume that detection requires two-instrument coincidence, implying (a) that the network's sensitivity is set by the second-most-sensitive detector, here assumed to be one of the advanced LIGO detectors operating in the zero detuned/high-power configuration (Aasi et al. 2013b); and (b) that for a calendar time T yr of operating time, the network accumulates only $p^2 T$ yr coincident time, where $p = 0.8$ is the duty cycle applied for the two most sensitive instruments. Using these assumptions, we anticipate that advanced LIGO will quote upper limits as a function of *detected* (redshifted) mass $M_{\text{tot},z}$ (in M_{\odot}) computed by the following expression:

$$\mathcal{R}_{aLIGO} = \frac{2.3}{V p^2 T} \text{Mpc}^{-3} \text{yr}^{-1}, \quad (21)$$

where V is the volume inside which a binary with the redshifted mass $M_{\text{tot},z}$ could be seen by the second-most sensitive detector, using the detection threshold $\text{SNR} = 8$ (see Eq. 2). Accounting for cosmology and orientation-dependent sensitivity, we evaluate this volume for each $M_{\text{tot},z}$ by first computing the maximum luminosity distance $D_{\text{hor}}(M_{\text{tot},z})$ to which the instrument is sensitive at that mass, using our detector sensitivity and a model for binary coalescence; using cosmology to find the associated horizon redshift z_{hor} ; and then evaluating the volume V with eq. 15. To eliminate the ambiguity with spin and mass ratio, for simplicity we assume all coalescing binaries have equal mass and zero spin: we evaluate $D_{\text{hor}}(M_{\text{tot},z})$ using an effective-one-body waveform model (EOBNRv2; Pan et al. 2011).

The upper limits obtained with the above detailed calculation are presented and contrasted with a simple intuitive estimate in Figure 2. For the simple estimate we scale the initial LIGO/Virgo upper limits (see Sec. 4.1) by a factor of 0.001, corresponding to an increase in the sampled volume by a factor $1000\times$ (and an increase in the horizon distance by a factor $10\times$) going from initial to advanced LIGO/Virgo. For low total merger mass ($\lesssim 25 M_{\odot}$) both methods give very similar upper limits. However, for higher total merger mass ($\gtrsim 25 M_{\odot}$) the simple estimate results in much deeper upper limits than expected for advanced LIGO/Virgo. Because advanced LIGO is sensitive to coalescing binaries at moderate to significant redshifts, an extrapolation of the initial LIGO upper limits must both increase sensitivity ($\times 10^{-3}$ on the y axis) and account for the difference between rest-frame and detected total mass (a mass-dependent shift of the x axis).

5. UPPER LIMITS VERSUS PREDICTIONS

5.1. Comparison of Models with Initial LIGO/Virgo Upper Limits

In Figures 3 and 4 and Tables 3 and 4 we present evolutionary model predictions for double compact object merger rate densities. The predictions are constructed with method II (see Sec. 2.2) and contrasted with observational initial LIGO/Virgo upper limits (see Sec. 4.1). Our models are described in Sec. 3. In what follows we list the most noteworthy trends, and compare directly predicted rate densities with the existing observational upper limits.

The dependence of the merger rate density on the total mass of the binary begins with a pronounced peak in the first mass bin ($M_{\text{tot},z} = 2\text{--}5 M_{\odot}$) where all of the NS-NS systems are found. It is possible that some BH-NS systems may contribute to this bin in model V4 (no mass gap). However, since our standard approach naturally produces a mass gap between NSs and BHs (BHs form with mass above $\sim 5 M_{\odot}$; see Belczynski et al. 2012) there are no BH-NS systems in this first bin for models V1, V2, V3. The next mass bin ($M_{\text{tot},z} = 5\text{--}8 M_{\odot}$) with relatively low merger rate densities and the two following bins (with total mass $M_{\text{tot},z} < 14 M_{\odot}$) contain predominantly BH-NS systems. Then higher mass bins are dominated by BH-BH mergers. This will be demonstrated below (see Sec. 5.2 and Fig. 7).

In models V1, V2, and V4 the merger rate density increases for these bins up to a total merger mass of $\sim 30 M_{\odot}$. At higher masses the merger rate density is steadily declining, but massive binary mergers are still predicted in all of our models up to a total redshifted mass of $\sim 120 M_{\odot}$.

Predictions for the model with high BH kicks (V3) show a different behavior than other models (V1, V2, V4). There is a rather flat merger rate density dependence on total merger mass for a broad spectrum of total redshifted masses ($10\text{--}110 M_{\odot}$). The dip for the lowest mass BH-NS bin ($M_{\text{tot},z} = 5\text{--}8 M_{\odot}$) is significantly more pronounced than in other models. These changes are naturally explained by high natal kicks applied to all BHs independent of their formation mass. The high natal kicks tend to disrupt potential progenitors of BH-BH and BH-NS mergers.

Predictions for the delayed SN engine model (V4) closely resemble the standard model (V2). The only notable difference comes in the second mass bin ($M_{\text{tot},z} = 5\text{--}8 M_{\odot}$) in which the V4 model generates a merger rate density almost as high as for our most optimistic model V1 (see Table 3 and 4). This relatively high merger rate density is produced by low mass mergers (either BH-BH or BH-NS) with compact objects with mass in the mass gap range ($2\text{--}5 M_{\odot}$) that are naturally formed within the evolutionary framework of model V4. We do not show this model to avoid overcrowding on the plots.

Generally, the merger rate density decreases from model V1 to V2 to V3. For example, for low metallicity evolution the merger rate density drops by a factor of a \sim few from V1 to V2, and then down by \sim one–two orders of magnitude from model V2 to V3. These changes are very similar for high metallicity evolution (see Table 4). The decreasing merger rate density progression is easily understood in terms of the input physics associated with our evolutionary models. Model V1 allows for very optimistic evolution in the context of double compact object formation (in ad-

dition to CE during core Helium burning, case B RLOF evolution allows the formation of close post-CE binaries). In model V2 the formation routes for close double compact objects are limited to case C RLOF (CE only during core Helium burning) and thus the merger rate densities decrease. Finally, the high BH kicks present in model V3 severely reduce the rate density for BH-BH and BH-NS mergers.

Model V1 merger rate densities for low metallicity evolution are the highest within our sample of models. In particular, the predicted merger rate densities are only a factor of 18 below the initial LIGO/Virgo upper limits in the $M_{\text{tot},z} = 25\text{--}37 M_{\odot}$ bin. The more realistic model V2 results in a BH-BH merger rate density a factor of ~ 70 below the initial LIGO/Virgo upper limits for a total merger mass of $M_{\text{tot},z} = 25\text{--}54 M_{\odot}$. For comparison, note that the predicted merger rate density in the lowest mass bin (NS-NS mergers) is a factor of ~ 1000 below the upper limits for all models and for both metallicity evolution scenarios. This indicates that BH-BH mergers are expected to be dominant GW sources within the framework of the evolution adopted in models V1, V2, and V4. If no detections are made after a modest increase of LIGO/Virgo sensitivity, these specific evolutionary models will be eliminated in the context of BH-BH formation.

Our calculations incorporate the evolution of average metallicity with redshift into the cosmological model of the Universe; a broad spectrum of metallicities is employed in our population synthesis rate predictions. Changing the details of the adopted metallicity evolution model, within the uncertainties, produces at best modest effects on the rate predictions. Specifically, the low metallicity models produce somewhat higher merger rate densities for heavy mergers (BH-BH) and somewhat lower merger rate density for low-mass mergers (NS-NS). These trends are understood in terms of the effects of metallicity on the BH-BH formation (low metallicity boosts the formation) and on the NS-NS formation (low metallicity suppresses the formation; see Dominik et al. 2012). For example, the standard model (V2) merger rate density changes from $1.3 \times 10^{-8} \text{ Mpc}^{-3} \text{ yr}^{-1}$ for low metallicity evolution (see Table 3 and Fig. 3) to $7.0 \times 10^{-9} \text{ Mpc}^{-3} \text{ yr}^{-1}$ for high metallicity evolution (see Table 4 and Fig. 4) for BH-BH mergers with total mass $M_{\text{tot},z} = 25\text{--}37 M_{\odot}$. The decrease of merger rate density from low to high metallicity evolution is rather moderate: only a factor of ~ 2 .

Note that metallicity itself plays a crucial role in the formation process of BH-BH binaries (Belczynski et al. 2007; Belczynski et al. 2010a). For example, a group of stars with solar metallicity will form $\sim 10\text{--}100$ times fewer BH-BH mergers than the same group with 10% solar metallicity (de Mink & Belczynski 2015). However, once we incorporate this very strong dependence into cosmological models of the Universe and employ a broad spectrum of metallicities (as in our methods II and III), the merger rate density predictions are not as strongly affected. Both metallicity evolution models generate (alas with a different efficiency) low metallicity stars (typical progenitors of BH-BH mergers). A broad BH-BH merger delay time distribution (Dominik et al. 2013, 2015) allows for both models to produce BH-BH binaries that will merge at low redshifts.

5.2. Comparison of Models with Forecasted Advanced LIGO/Virgo Upper Limits

In Figures 5 and 6 and Tables 5 and 6 we present evolutionary model predictions for double compact object merger rate densities. The predictions are constructed with method II (see Sec. 2.2) and contrasted with the forecasted advanced LIGO/Virgo upper limits (see Sec. 4.2). Our models are described in Sec. 3.

The predicted double compact object merger rate density within the volume sampled by the advanced LIGO/Virgo detectors are high enough relative to the forecasted upper limits to make detections very likely for most of our considered evolutionary models: V1, V2, and V4 for both metallicity evolution scenarios. Model V4, which is not shown in the figures, is very similar to model V2 (and V4 merger rate densities are given in the tables). Predictions for model V3 are well below the upper limits in all mass bins, with the exception of the NS-NS mass bin ($2-5 M_{\odot}$). This does not make detections impossible, it just indicates that the detections are highly unlikely for this evolutionary scenario. The difference between predictions and the upper limits is a gauge of how likely (or unlikely) the detections will be. In the case of models V1, V2 and V4 the detections are highly likely, as merger rate densities are well above the upper limits in some mass bins. If there is no detection, these models can be reliably excluded as incorrect. For our standard input physics and low-metallicity evolution (model V2l), the three mass bins that are the highest above the advanced LIGO/Virgo upper limits are: $M_{\text{tot},z} = 25-37 M_{\odot}$, with merger rate density is 5.0 times above upper limits; $M_{\text{tot},z} = 37-54 M_{\odot}$, with merger rate density is 12.5 times above upper limits; $M_{\text{tot},z} = 54-73 M_{\odot}$, with merger rate density is 6.4 times above upper limits (see Table 5). This indicates the most likely mass range for future detections. This is a generic feature of our predictions found in most models (V1, V2, V4) for both metallicity evolution scenarios. The only exception is model V3 with high BH natal kicks, with merger rate density consistently below the upper limits. Note that our comparison is done for one year of observations (that is how upper limits are calculated). The advanced LIGO/Virgo detectors are scheduled to work for approximately ~ 10 years at full sensitivity. However, even if we made the upper limits better by a factor of 10, model V3 merger rate densities for BH-NS and BH-BH mergers would still end up below the improved 10 year upper limits.

Note that our predictions are close to the upper limits for all the models of NS-NS mergers (the first mass bin). This makes detections questionable, but not impossible, within 1 year of observation, but quite likely within 10 years.

The results for the advanced detectors may be contrasted with the predictions for initial LIGO/Virgo: all the models are below the upper limits. This difference comes from two facts. First, the advanced instruments will be much more sensitive (by a factor of ~ 10), so the upper limits (per unit of observation time) will be associated with much larger searched volume (~ 1000) than initial LIGO/Virgo. Second, the predicted merger rate densities within the volumes sampled by the advanced instruments are generally higher than those predicted for volumes sam-

pled by the initial instruments. Initially, merger rate densities increase with increasing redshift to $z = 1-4$ (depending on the type of merger), and then they decline with redshift (Dominik et al. 2013; see their Fig. 3 and 5). This is a result of the merger rate density approximately following star formation rate (that peaks at $z \approx 2$) and the contribution of mergers that are formed at high redshifts in low metallicity stellar populations with long delay times. This effect becomes more pronounced with total merger mass as more massive mergers can be detected from higher redshifts. In particular, for our standard model V2 and low metallicity evolution, the difference in merger rate density is negligible for NS-NS mergers ($5.0 \times 10^{-8} \text{ Mpc}^{-3} \text{ yr}^{-1}$ for initial LIGO/Virgo versus $5.7 \times 10^{-8} \text{ Mpc}^{-3} \text{ yr}^{-1}$ for advanced LIGO/Virgo); it becomes more pronounced for $M_{\text{tot},z} = 37-54 M_{\odot}$ ($4.5 \times 10^{-9} \text{ Mpc}^{-3} \text{ yr}^{-1}$ for initial LIGO/Virgo versus $1.5 \times 10^{-8} \text{ Mpc}^{-3} \text{ yr}^{-1}$ for advanced LIGO/Virgo); and it is significant for higher mass bins (e.g., for $M_{\text{tot},z} = 91-109 M_{\odot}$ it is $1.6 \times 10^{-11} \text{ Mpc}^{-3} \text{ yr}^{-1}$ for initial LIGO/Virgo versus $4.5 \times 10^{-10} \text{ Mpc}^{-3} \text{ yr}^{-1}$ for advanced LIGO/Virgo).

We also note that all our model predictions extend to very high total redshifted merger mass: $\sim 400 M_{\odot}$ for models V1, V2, V4 and $\sim 350 M_{\odot}$ for model V3. We have already explained this surprising finding (Sec. 2.4) in the context of model V2. A very low metallicity progenitor ($Z = 0.0001$) binary with very high initial component masses ($m_{\text{zams},1} = 148 M_{\odot}$ and $m_{\text{zams},2} = 144 M_{\odot}$) forms a massive BH-BH system (intrinsic total BH-BH mass of $136 M_{\odot}$) that merges at redshift $z = 2$ (total redshifted mass of $\sim 400 M_{\odot}$). Such a merger is potentially detectable at full advanced LIGO/Virgo sensitivity with the use of the full waveform (inspiral-merger-ringdown). Models V1 and V4 show the same final outcome. For model V3 high BH natal kicks disrupt a large number of BH-BH progenitors and the most massive binaries (with associated small number statistics) are not found in our Monte Carlo population synthesis simulations.

BH-NS mergers provide only a relatively small contribution to high mass bins for models V1, V2 and V3 and moderate contribution to high mass bins for model V4. This is demonstrated in Figure 7. BH-NS mergers occupy mass bins in the range $M_{\text{tot},z} = 5-73 M_{\odot}$ for models V1, V2, V3 and $M_{\text{tot},z} = 2-127 M_{\odot}$ for model V4. The highest merger rate densities for these mergers are found in the mass range $M_{\text{tot},z} = 8-17 M_{\odot}$ for models V1, V2, V3. For model V4 the highest three bins include total redshifted merger mass in the range $M_{\text{tot},z} = 2-5 M_{\odot}$ and $M_{\text{tot},z} = 25-54 M_{\odot}$. Both our optimistic model (V1) and delayed SN engine model generate merger rate densities that are at the level of (or higher than) the upper limits (1 yr of observations). The standard model (V2) merger rate densities for BH-NS binaries are about an order of magnitude below the upper limits, making detections unlikely during 1 yr and likely during 10 yr of observations. Model V3 merger rate densities are quite low and make BH-NS detections unlikely.

In summary: the predictions, within optimistic-to-realistic models, show likely detections for NS-NS mergers (first mass bin), possible detections for BH-NS mergers (second and higher mass bins), and very likely detections for BH-BH mergers (third and higher mass bins) at the

full advanced LIGO/Virgo sensitivity. Pessimistic model indicates likely detections for NS-NS mergers and unlikely detections for BH-NS and BH-BH mergers.

6. BLACK HOLE NATAL KICKS

We have compiled the empirical and theoretical information on BH natal kicks. The empirical data is presented in Table 7 and Figure 8 and discussed in Sections 6.1 to 6.9. The discussion of physics behind natal kicks is given in Sec. 6.10.

6.1. Natal Kicks From Galactic Positions: I

Repetto & Nelemans (2015) have studied natal kicks in seven Galactic BH low mass X-ray binaries (BH LMXBs) with very short periods (< 1 d; thus only with main sequence donors). These include: GRO J0422+32, GRS 1009-45, A 0620-00, GS 2000+251, GRS 1124-68 (Nova Mus 91 in their paper), XTE J1118+480, H 1705-250. The Galactic plane ($h_z = 0$ kpc) was assumed to be the birth place of these binaries. Positions of these binaries above the Galactic plane (h_z) along with a simple model of binary physics were used to estimate lower limits on natal kicks. The results indicate rather low natal kick lower limits for five systems ($\lesssim 60$ km s $^{-1}$), while for one system (XTE J1118+480) the lower limit is somewhat higher (~ 100 km s $^{-1}$) and for another one (H 1705-250) the lower limit is very high (~ 400 km s $^{-1}$). It was concluded that BHs can receive both low and high natal kicks and that natal kicks do not correlate with BH mass within this small subpopulation of BH systems. The results were found for binaries reported to host BHs with mass in the range: 3.0–8.8 M_\odot .

The BH masses may be potentially revised to a higher range: from 5 to above 10 M_\odot (see our Table 7). The BH mass of GRO J0422+32 was revised from 3–5 M_\odot (Gelino & Harrison 2003) to a mass larger than 10 M_\odot (Reynolds et al. 2007). Both estimates are based on different information to establish inclination (and thus BH mass) of this binary. The former estimate is based on the best observations of ellipsoidal modulations, while the latter employs the best estimate of the disk contribution (found at $\sim 30\%$ level) to the light curve. The BH mass of GRS 1009-45 estimated at first at 4.4 M_\odot (Filippenko et al. 1999), was later revised with new spectroscopic and photometric observations to 8.5 M_\odot (Macias et al. 2011). This revised range of BH masses does not require BHs within the mass gap, and it includes both Galactic low mass BHs (5–10 M_\odot) and high mass BHs (10–15 M_\odot).

H 1705-250, depending on the large distance estimate uncertainty (6.5–10.7 kpc), is located at $h_z = 1.0$ –1.7 kpc above the Galactic plane right in the bulge region. Since the bulge scale height of stars is about 0.7 kpc (e.g., Juric et al. 2008; SDSS data), there is a non-negligible probability that H1705-250 was born at (or nearby) its current location. The donor star in this system is a low mass main sequence star (~ 0.15 –1.0 M_\odot ; Martin et al. 1995, Filippenko et al. 1997), thus it cannot be excluded that this system was born longer than 10 Gyr ago in the bulge, with no natal kick needed to place the binary where it is found today. On the other hand, it can not be excluded that this system was born in the thin disk as assumed by Repetto & Nelemans (2015). The thin disk current scale

height is ~ 0.3 kpc (Juric et al. 2008), and the most likely scale height for the formation of X-ray binaries is ~ 0.1 kpc (e.g., Brandt & Podsiadlowski 1995). The calculation of Repetto & Nelemans (2015) with the assumed initial position of binary at the Galactic plane ($h_z = 0$ kpc) resulted in a minimum natal kick of 415 km s $^{-1}$ for the BH in H 1705-250. However, there was a mistake in this estimate (S.Repetto, private communication 2015) and the corrected lower limit is now set at 217 km s $^{-1}$. We keep this estimate and mark it with a point and upward arrow in Figure 8, to indicate a lower limit that corresponds to the initial location of this system at the Galactic plane. But we also allow for the possibility that this system was born in the bulge without a natal kick: we mark our potential revision of the Repetto & Nelemans (2015) estimate with a line going all the way down to 0 km s $^{-1}$.

The other five systems (GRO J0422+32, GRS 1009-45, A 0620-00, GS 2000+251, GRS 1124-68) have small estimated distances from the Galactic plane: $h_z < 0.8$ kpc (Repetto & Nelemans 2015). All of these systems host currently low mass donors (typically $\sim 0.5 M_\odot$ stars; <http://www.stellarcollapse.org/bhmasses>), so it can not be excluded that they were born longer than 11 Gyr ago in the thick disk. Since the thick disk current scale height is 1 kpc (e.g., Juric et al. 2008) all these systems could have been potentially born at (or near) their current location. This would imply no natal kick needed for BHs in these binaries. However, the donor stars in these binaries may have started with much higher mass ($\gtrsim 1 M_\odot$) making them younger than the thick disk population, or the thick disk was initially much more compact (in vertical scale) than today. In such cases the estimates of Repetto & Nelemans (2015), that place these binaries in the Galactic plane, are correct. As in the case of H 1705-250 we mark both possibilities in our Figure 8 and Table 7.

The only exception (in the Repetto & Nelemans 2015 sample) from this systematic uncertainty on the initial source position is XTE J1118+480 located at a distance of 1.6–1.8 kpc and at $h_z = 1.4$ –1.6 kpc above the Galactic plane (so it is not in the bulge nor the thick disk). However, the estimate based only on its position is superseded by one that includes its known 3D velocity (see Sec. 6.4).

6.2. Natal Kicks From Galactic Positions: II

There are four additional BH binaries with natal kick lower limits derived from their positions in the Galaxy studied by Repetto, Davies and Sigurdsson (2012). In this work, Repetto et al. (2012) computed the minimum natal kick needed in order to place the binary at the current height from the Galactic plane. They assume the binary to be born in the Galactic plane (at $h_z = 0$ kpc), and they take the central value of the distance to the BH systems to calculate their current positions above the Galactic plane. Unlike the work by Repetto et al. (2015), they do not follow the binary evolution of the BH systems, but rather they take average binary properties.

Here we revise their estimates accounting for the scale height of the disk, and allowing for uncertainty of the distance estimate. Note that in a different part of their study, Repetto et al. (2012) have carried a binary population synthesis calculation and allowed for a spread of initial positions of progenitor binaries in the thin disk with a scale height of 0.167 kpc. They followed motion of binaries in

the Galactic potential to check what natal kick distribution is needed to recover overall h_z -distribution of the BH binaries. This part of their study was not used to estimate natal kick lower limits for particular binaries and we do not use it.

In the case of XTE J1550-564 ($h_z = -0.12$ to -0.15 kpc, $M_{\text{opt}} = 0.3 M_{\odot}$ is the current mass of a donor star), this binary has a small distance from the Galactic plane, which is compatible with the formation within the scale height h of the disk where X-ray binaries are formed ($h \sim 0.1$ kpc; Brandt & Podsiadlowski 1995), and which does not require a natal kick at birth. We therefore revise the lower limit of 10 km s^{-1} calculated by Repetto et al. (2012), pushing it down to 0 km/s .

In the case of GS 2023+338, the 3D peculiar velocity was measured and a better estimate of the natal kick may now be obtained, superseding the value presented in Repetto et al. (2012). See the discussion in Sec. 6.5.

In the case of XTE J1819-254 ($h_z = -0.63$ to -1.03 kpc; the spread in h_z reflects uncertainty on distance estimate) its average height from the Galactic plane ($h_z = -0.83$ kpc) lead to a natal kick estimate of 190 km s^{-1} in Repetto et al. (2012). The companion star to the BH has a mass $M_{\text{opt}} = 5.5$ – $8.1 M_{\odot}$ and a spectral type and luminosity class: B9III (<http://www.stellarcollapse.org/bhmasses>). Its age being young (< 100 Myr), one can exclude its origin in thick disk or bulge. We therefore place the progenitor at $h_z = 0.3$ kpc that corresponds to the current scale height of the thin disk (Juric et al. 2008). We then follow the same analysis as Repetto et al. (2015) to estimate the minimum binary center-of-mass velocity to move it to the minimum height estimated for the current position of this system at $h_z = -0.63$. This velocity is assumed to be entirely in $-h_z$ direction and the motion is tracked in Galactic potential. Our estimate: 100 km s^{-1} provides a conservative lower limit on BH natal kick. The natal kick has to be larger than the binary center-of-mass velocity, as natal kick is received by a $\sim 10 M_{\odot}$ BH while the center-of-mass velocity operates on entire binary with mass of $\gtrsim 15 M_{\odot}$.

In the case of 4U 1543-47 ($h_z = 0.70$ kpc, $M_{\text{opt}} = 2.3$ – $2.6 M_{\odot}$; A2V), with the optical component/donor star maximum age of ~ 1 Gyr, the thick disk or bulge origin may be eliminated. Repetto et al. (2012) have set a lower limit on natal kick (80 km s^{-1}) assuming the binary is formed right at the Galactic plane ($h_z = 0$ kpc). Using the same arguments as in the case of XTE J1819-254, we reset this lower limit to 75 km s^{-1} .

For XTE J1550-564, XTE J1819-254 and 4U 1543-47, we keep original Repetto et al. (2012) estimates, but we mark our modest revisions both in Table 7 and in Figure 8.

6.3. Natal Kick From 3D Velocity: GRO J1655-40

Willems et al. (2005) have performed analysis of available evolutionary, nucleosynthetic and proper motion constraints for GRO J1655-40. They have backtracked 3D motion and evolution of this binary to the time of BH formation in the Galactic potential to estimate post supernova velocity. This post supernova velocity was in turn used to estimate the magnitude of a BH natal kick. The estimated 3D post supernova velocity (45 – 115 km s^{-1}) may potentially lead to much smaller natal kick velocity, than

earlier estimates based just on present-day radial velocity (-114 km s^{-1} ; corrected for the Sun motion and Galactic differential rotation).

Evolutionary predictions along with Galactic motion constraints yield a wide range of BH natal kick values: 0 – 210 km s^{-1} . Willems et al. (2005) quote this range for BH mass ($5.4 M_{\odot}$) adopted from Beer & Podsiadlowski (2003). We chose this model as this mass was later confirmed by X-ray timing analysis (Motta et al. 2014; $5.31 \pm 0.07 M_{\odot}$). Note that symmetric supernova scenario (0 km s^{-1} natal kick) is allowed in this solution and that the present-day 3D velocity is fully accounted for by the Blaauw kick (Blaauw 1961; extra systemic velocity just from mass loss during BH formation) and Galactic orbit of GRO J1655-40. Also, note that the largest allowed BH natal kick is just half of what is estimated for Galactic pulsars (420 km s^{-1} ; average NS 3D natal kick from Hobbs et al. 2005).

Additional, supernova/nucleosynthetic constraints led Willems et al. (2005) to impose a somewhat more stringent constraint on the BH natal kick: 40 – 140 km s^{-1} . This conclusion was based on detection of enhanced abundance of some heavy elements (O, Mg, S, Si, Ti; 10 times solar) in the GRO J1644-40 low-mass donor star spectrum. These overabundances were used to argue for supernova (with its mass loss assumed to have polluted companion star) to form the BH in GRO J1644-40 (Israelian et al. 1999). Willems et al. (2005) have used 1D supernova models (Fryer et al. 1999) to estimate that only helium stars in narrow mass window 8 – $10 M_{\odot}$ may both produce $\sim 5 M_{\odot}$ BH with enough asymmetry to deposit the heavy elements in the GRO J1644-40 optical star. The limits on helium star mass enabled to narrow down the “successful” evolutionary sequences (and natal kicks) leading to the formation of binaries resembling GRO J1644-40.

Supernova models with the associated nucleosynthetic yields employed by Willems et al. (2005) in fact produce titanium farther out from the exploding star center for the massive helium star model ($10 M_{\odot}$) as compared with the lower mass model ($6.2 M_{\odot}$). Thus they allow for easier deposition of this element in the companion atmosphere (see their Fig.10). However, in both models, iron production shows very similar trend as titanium does. If we are to believe the models and arguments presented by Willems et al. (2005) there should be an overabundance of iron on par with the observed overabundance of titanium. However, the same observations used to measure the overabundance of titanium resulted with approximately solar iron abundance in GRO J1644-40 ($[Fe/H] = 0.1 \pm 0.2$; Israelian et al. 1999).

Willems et al. (2005) “successful” evolutionary sequences are based on details of RLOF calculations and response of the donor to mass loss. Some of their sequences show that RLOF could be initiated in eccentric binaries (e.g., their Fig. 5), but they are circularized and synchronized instantaneously (“by hand”) at the onset of RLOF. However, it is not clear how to treat such cases. It seems that for some binary configurations RLOF may rather quickly circularize the orbit, while for others the eccentric periodic mass transfer at periastron may be a rather prolonged phase (Sepinsky et al. 2010).

The mass loss from the optical star in GRO J1644-40

was quite significant in models presented by Willems et al. (2005). The evolutionary sequences allowed for a change of initial star mass from 2.3–4.0 M_{\odot} down to 1.45 M_{\odot} . Such a significant mass loss and its effects on star evolution (apparent aging, decrease in burning rates, radius evolution and its visual properties) are not fully understood. This just reflects the fact, that the stellar models are still subject to large uncertainties arising from treatment of convection, mixing and rotation. For example, some particular stellar models were adopted for Willems et al. (2005) estimates (e.g., models without rotation and with moderate convection; Ivanova et al. 2003), but the systematic uncertainties involved in stellar evolution were not tested.

The significant mass loss predicted by Willems et al. (2005) models and the fact that donor star is massive enough to have radiative envelope (not as much mixing as in case of convective envelope) it is surprising that observed overabundance of elements is considered to be a deposition from supernova explosion. The significant RLOF mass loss should have removed the polluted outer layers from the donor star. It seems that either the donor star has not lost significant mass in RLOF (and the models are incorrect) or that the observed overabundances are not connected to supernova explosion that has formed the BH in this system.

Despite of the evolutionary uncertainties Willems et al. (2005) is at the moment the most thorough and detailed study of BH natal kick in GRO J1644-40. Due to the caveats discussed above we are hesitant to use the more stringent constraints on BH natal kick. We chose to adopt the wider range presented by Willems et al. (2005). It is very informative, and possibly contrary to some preconceptions in the community, that the BH in this system is allowed to have formed *without* any natal kick (0 km s^{-1}). At best, this BH has formed with a *moderate* natal kick (210 km s^{-1}).

6.4. Natal Kick From 3D Velocity: XTE J1118+480

Fragos et al. (2009) have studied available constraints, 3D peculiar velocity included, on the past evolution of XTE J1118+480. Using methods very similar to the ones employed for GRO J1655-40 (Willems et al. 2005) the past history and the BH natal kick were reconstructed. The major difference between the two studies comes from the fact that nucleosynthetic information was not used to constraint the natal kick by Fragos et al. (2009) as the abundance measurements for XTE J1118+480 do not show such striking features as in the case of GRO J1655-40. This actually makes this case stronger (see Sec. 6.3 for discussion of issues with nucleosynthetic constraints).

Fragos et al. (2009) estimated that current properties of the system, with its 3D peculiar velocity, combined with RLOF sequences and evolutionary predictions for low mass MS donors, constrain the BH natal kick in XTE J1118+480 to: 80–310 km s^{-1} . This estimate has two potential caveats, both discussed by authors.

The wider set of donor stars could be potential progenitors of donor stars than considered by Fragos et al. (2009; only MS stars with mass $< 1.6 M_{\odot}$). Intermediate mass donors ($\sim 3\text{--}5 M_{\odot}$) were also proposed to be potential progenitors of BH low-mass X-ray binaries (e.g., Justham, Rappaport & Podsiadlowski 2006). However, models of

such massive donors (stripped from most of their mass by RLOF) seem not to match effective temperatures of observed stars, while Fragos et al. (2009) can match the temperature of donor in case of XTE J1118+480. If somehow BH LMXBs originated from intermediate mass donors, that would lead to different evolutionary constraints on the formation of XTE J1118+480 and thus affect constraints on BH natal kick.

Fragos et al. (2009) assumed that the system originated in the Galactic thin disk and that the donor star had solar metallicity. This assumption, coupled with significant 3D peculiar velocity and its current position in halo, led directly to the estimate of high natal kick for XTE J1118+480. The alternative scenario, that does not require significant natal BH kick (if any natal kick at all), allows for the formation of this system in halo. Although this scenario can not be excluded, it does not seem very likely. Only two Galactic globular clusters have solar metallicity: Terzan 5 and Liller 2 (e.g., Harris 1996). More convincingly, Gonzalez Hernandez et al. (2006) detected super-solar abundances in the donor atmosphere. In a follow-up study, Gonzalez Hernandez et al. (2008) explored a series of SN explosion models in order to match the observed abundances of the donor atmosphere. They found the best match for a donor born in the Galactic thin disk, hence with solar metallicity, and later polluted with the ejecta of the exploding companion. A birth in the halo provided instead unacceptable fits to the observed abundances.

6.5. Natal Kick From 3D Velocity: GS 2023+338 (V404 Cyg)

GS 2023+338 is the system qualitatively resembling GRS 1915+105 (see Sec. 6.6). It consists of a $9 M_{\odot}$ BH with a low mass and evolved companion ($M_{\text{opt}} \sim 0.5\text{--}1.0 M_{\odot}$; K0/3 IV <http://www.stellarcollapse.org/bhmasses>) on a rather large orbit ($P_{\text{orb}} = 6.5\text{d}$). Miller-Jones et al. (2009a) presented parallax determination, that led to a revised distance to the source ($2.39 \pm 0.14 \text{ kpc}$). Using this precise distance estimate they have used radial velocity and proper motion known for this system to derive 3D peculiar velocity of $39.9 \pm 5.5 \text{ km s}^{-1}$. Miller-Jones et al. (2009a) concluded that the Galactic plane component of this velocity: 39.6 km s^{-1} is well above dispersion velocity in the position of GS 2023+338 (18.9 km s^{-1}). This implies that the GS 2023+338 3D peculiar velocity (or some significant part of it) originates from the BH formation. They also argued that Blaauw kick is most likely responsible for this 3D peculiar velocity, with natal kick (if any) being small.

We disagree with the above conclusion. In fact, it is allowed that the Blaauw kick (just symmetric mass loss) from the system produces peculiar velocity of $\sim 40 \text{ km s}^{-1}$ and that would require mass loss at supernova at the level of $5\text{--}10 M_{\odot}$ (e.g., Miller-Jones et al. 2009b). However, it is also allowed that this $9 M_{\odot}$ BH has formed without any significant mass loss as BH formation mechanism is not yet fully understood. If this was the case than natal kick could have provided most of the peculiar velocity (with some correction for potential contribution from dispersion velocity). Therefore, we adopt a range of $0\text{--}45 \text{ km s}^{-1}$ for the value of natal kick in GS 2023+338; from no natal kick to the maximum estimate on peculiar velocity from

Miller-Jones et al. (2009a).

6.6. *Natal Kick From 3D Velocity: GRS 1915+105*

Dhawan et al. (2007) have obtained the estimate of 3D peculiar velocity from parallax and proper motion measurements for GRS 1915+105. For the revised distance to the source (7–10.6 kpc; Reid et al. 2014) the 3D peculiar velocity was estimated at the level of $\sim 45\text{--}75 \text{ km s}^{-1}$ (see Fig.3 of Dhawan et al. 2007). Such a small velocity was interpreted as a result of Galactic velocity diffusion implying BH natal kick of 0 km s^{-1} . Another measurement of GRS 1915+105 proper motion and parallax translated to a peculiar 3D (non-circular/corrected for Galactic rotation) velocity of $22 \pm 24 \text{ km s}^{-1}$ and a 95% confidence upper limit of 61 km s^{-1} (Reid et al. 2014).

Since there is no comprehensive study of GRS 1915+105 evolution and motion in Galaxy we adopt the upper limit on peculiar 3D velocity as an upper limit on natal kick velocity (no diffusion, and no mass loss at BH formation assumed) and we allow for the no-natal-kick possibility (the diffusion scenario, or entire peculiar velocity from Blaauw kick assumed). The range for natal kick in GRS 1915+105 is then: $0\text{--}75 \text{ km s}^{-1}$. This is only an approximation as natal kick may have been higher than the upper value of peculiar velocity in case the Blaauw kick and natal kick worked in opposite directions.

Systemic peculiar velocity changes (in quasi-periodic way) in time as binary moves on its complex orbit in Galactic potential. For example, in the case of XTE J1118+480 the peculiar 3D velocity changes from $\sim 100 \text{ km s}^{-1}$ to $\sim 200 \text{ km s}^{-1}$ during motion of this binary in Galaxy (Fragos et al. 2009). GRS 1915+105 is on more circular and at lower h_z orbit (e.g., Dhawan et al. 2007) than XTE J1118+480 so the changes are not expected to be as drastic. However, the GRS 1915+105 peculiar velocity may have been much higher right after the BH formation and then it was gradually “thermalized” by interactions with much slower stars. After all, GRS 1915+105 moves in the relatively dense Galactic disk and it was very likely formed many Gyr ago (e.g., Belczynski & Bulik 2002). This just demonstrates the dangers of using the present day 3D peculiar velocity as a proxy for natal kick (as we do in the case of GS 2023+338 or GRS 1915+105) or as a starting point for BH natal kick estimates (e.g., Willems et al. 2005 or Fragos et al. 2009).

6.7. *Natal Kick From 3D Velocity: Cyg X-1*

Wong et al. (2012) have studied evolution and dynamics of 3D motion of Cyg X-1 based on parallax measurement of Reid et al. (2011). They have used the same method as Willems et al. (2005) and Fragos et al. (2009) in study of GRO J1655-40 and XTE J1118+480, respectively. Using position of this system in Galaxy, its radial velocity and its proper motion Wong et al. (2012) traced this system back in time to the moment of BH formation. The system was found to be $h_z = 30\text{--}110 \text{ pc}$ above Galactic plane and move with peculiar 3D velocity of $22\text{--}32 \text{ km s}^{-1}$ right after BH formation. Allowing for mass ejection and natal kick at the BH formation, it was found that BH in Cyg X-1 may have formed with or without natal kick. The allowed range for natal kick is rather broad $0\text{--}115 \text{ km s}^{-1}$, with a peak probability of 20 km s^{-1} .

Mirabel & Rodrigues (2003) argued that Cyg X-1 was born in Cyg OB3 association of massive stars due to their proximity and very similar motion on the sky. The space velocity of Cyg X-1 in respect to the association was estimated at $9 \pm 2 \text{ km s}^{-1}$. Wong et al. (2012) redid their analysis under assumption that the peculiar velocity of Cyg X-1 right after the BH formation is $\leq 10 \text{ km s}^{-1}$. The allowed range for natal kick is found in the range $0\text{--}60 \text{ km s}^{-1}$. Probability distribution of natal kicks is not given in this case by Wong et al. (2012).

It can not be excluded that Cyg X-1 has originated from some other place than Cyg OB3 association. However, the circumstantial evidence; similar distance, similar motion and the fact that massive stars are typically born in associations seems to be very convincing. Therefore, we adopt a natal kick range of $0\text{--}60 \text{ km s}^{-1}$ that corresponds to the origin of Cyg X-1 in Cyg OB3 association.

6.8. *Natal kicks for extragalactic BHs*

Note that there is one natal kick estimate ($< 130 \text{ km s}^{-1}$; Wong et al. 2014) for an extragalactic X-ray binary IC10 X-1 with a potentially very massive BH ($\sim 20\text{--}30 M_\odot$; Prestwich et al. 2007; Silverman & Filippenko 2008). Since this system does not enter our comparative analysis presented in the next section (Sec. 6.9), we do not discuss this case in detail.

BH mass estimate for this system is based on semi-amplitude of HeII 4685.8Å emission line (e.g., Prestwich et al. 2007). This line is expected to form in vicinity of hot W-R star (high ionization threshold) and trace its orbital motion. However, the accreting compact object may ionize significant part of W-R wind in which this line forms. It is then possible that the line will form not only in vicinity of W-R star but also in other sectors of binary affecting mass estimates of binary components (van Kerkwijk et al. 1996). This is why we call the compact object in IC10 X-1 only a “potentially” very massive BH.

6.9. *Comparison of Empirical Estimates with Models*

In this section we will contrast the empirically derived information on BH masses and natal kicks with population synthesis models of Galactic BH interacting binaries.

In one approach to BH natal kicks in core collapse SNe we employ the modified (decreased) Maxwellian kick distribution with $\sigma = 265 \text{ km s}^{-1}$. The mass of the remnant object generates gravitational potential strong enough to prevent parts or all of the mass ejected during SN from reaching escape velocity. The matter falling back onto the remnant object will reduce the original (Maxwellian) kick velocity due to conservation of momentum. The more massive the final (pre-SN) core of the star, the more fallback it generates. This results in BH natal kicks smaller than the NS kicks. To account for this effect we use a simple linear relation for the reduction of the natal kick magnitude by the amount of fallback during a SN:

$$V_k = V_{max}(1 - f_{fb}), \quad (22)$$

where V_k is the final magnitude of the natal kick, V_{max} is the velocity drawn from a Maxwellian kick distribution, and f_{fb} is the fallback factor. The values of f_{fb} range between $0\text{--}1$, with 0 indicating no fallback/full natal kick and 1 representing total fallback/no kick (direct BH formation

without any SN event and without any mass loss). Additionally to the natal kick, the Blaauw kick is calculated from symmetric mass ejection (if any). The combination of two kicks may disrupt the binary, or generate a peculiar systemic velocity of the surviving binary in its motion in Galaxy. The values for the fall back and BH masses for our models are introduced and described in Fryer et al. (2012). This approach to natal kicks is adopted in our models V1, V2 and V4 and we refer to this scenario as “low BH kicks”. This method generates a trend of natal kicks decreasing with BH mass. In particular massive BHs do not receive any natal kick.

In another approach to BH natal kicks we draw a Maxwellian 1D velocity distribution with $\sigma = 265 \text{ km s}^{-1}$ independent of BH mass. This distribution of natal kicks is based on the observed velocities of single Galactic pulsars (Hobbs et al. 2005). Such a distribution allows for very high BH natal kicks with the averaged 3D natal kick magnitude of 420 km s^{-1} . The kick direction is assumed to be random. We refer to this scenario as “high BH kicks” and employ this scheme in our evolutionary model V3. Note that this model allows for low natal kicks. In particular, our evolutionary model will eliminate the highest kicks drawn from this distribution by disrupting binary stars.

In Figure 8 we show empirical estimates of the BH natal kicks and BH masses. Both the BH natal kicks and the mass estimates suffer large uncertainties. Along with the empirical estimates we show two theoretical evolutionary predictions of Galactic population of interacting BH binaries. The two models differ only in one assumption; either low or high BH kicks are adopted. The models are calculated for stars with solar metallicity ($Z = 0.02$) and with our standard evolutionary model (see Sec. 3). We stop evolution at the point of BH formation. We choose only binaries with orbital separations smaller than $100 R_{\odot}$. The longest period BH binary in our empirical sample (GRS 1915+105) has period of $P_{\text{orb}} = 33.5 \text{ d}$ (Greiner, Cuby & McCaughrean 2001) that corresponds to the orbital separation of $\sim 100 R_{\odot}$. We then assume that each of these binaries will eventually undergo RLOF and become an X-ray binary. We do not model RLOF phase (there seem to be a general issue with Galactic BH binary modeling; i.e., Wiktorowicz et al. 2014). Instead we assume that some fraction (randomly chosen value between 0 and 0.2) of the donor star can accrete onto a BH. We plot the BH masses increased in this process versus the natal kicks these BHs have been assigned in our “low-kick” or “high-kick” scenario (Fig. 8). In this approach we have not taken into account any potential observational biases as we lack a good model for X-ray emission for BH systems. This is in particular true for BH transients that make most of our sample (all, but Cyg X-1, systems in Table 7 are transients).

Note that our evolutionary models take into account various binary configurations at the time of BH formation, and account for survival and disruptions of systems on arbitrary orbits. Only systems that are tightly bound or those that receive small or preferably oriented natal kicks survive BH formation. We note a number of very small (or no) natal kick binaries and with kicks generally below 300 km s^{-1} for our low BH kick model. For high BH kick model, the kicks in surviving binaries are non-

negligible, with most found in range $50\text{--}500 \text{ km s}^{-1}$. As clearly seen from Figure 8, while neither of the models provides a good match to the empirical estimates, both models are consistent with the empirical estimates (i.e., we can find synthetic binaries nearby each empirical point for both natal kick models). On one hand this reflects the fact that the empirical data is still very poor (only 5 good estimates and many weak lower limits). On the other this demonstrates that even low-kick model may deliver a range of BH natal kicks that are consistent with the empirical estimates. For low-mass BHs there is significant mass ejection so both low and high kicks are expected depending on the level of asymmetry. For high mass BHs, low to zero kicks are expected if a BH forms with high mass (small to no mass ejection) and higher kicks are expected for a BH that has formed at low mass and then increased its mass via accretion from its companion. For high BH kick model (despite its name) low kicks at the level of $\sim 50 \text{ km s}^{-1}$ are predicted in our evolutionary simulations for some of the interacting BH binaries since BH natal kicks are drawn from the Maxwellian distribution.

Contrary to some common beliefs that natal kicks decrease with BH mass, we point out that both theoretical models: natal kicks independent of BH mass (our high-kick model) and kicks decreasing with BH mass (our low-kick model), can explain the empirical data within their associated errors. In particular, Mirabel & Rodrigues (2003) and Dhawan et al. (2007) claim that the most massive BHs in Galaxy (GRS 1915+105; $M_{\text{BH}} = 12.4 M_{\odot}$ and Cyg X-1; $M_{\text{BH}} = 14.8 M_{\odot}$) form at dark (without a supernova) and without any significant natal kick, while lower mass BHs (e.g., XTE J1118+480; $M_{\text{BH}} = 7.6 M_{\odot}$) form at supernova with significant mass ejection asymmetry and associated high natal kick. This is at first glance very convincing, however other systems may challenge such notion. For example, GS 2023+338 with $M_{\text{BH}} = 9.0_{-0.6}^{+0.2} M_{\odot}$ has very small natal kick $V_{\text{kick}} < 45 \text{ km s}^{-1}$, while more massive BH in XTE J1819-254 ($M_{\text{BH}} = 10.2 \pm 1.5 M_{\odot}$) has significant natal kick $V_{\text{kick}} > 100 \text{ km s}^{-1}$. Apparently, this counter-example may go away if errors on BH mass estimates are allowed to work in favor of Mirabel & Rodrigues (2003) and Dhawan et al. (2007) claims. If one applied similar type of arguments on allowed errors on natal kicks, it may be claimed that the second lowest mass BH on our list: GRO J1655-40 ($M_{\text{BH}} = 5.3 \pm 0.3 M_{\odot}$) formed with no natal kick, while the two heaviest BHs (in Cyg X1 and GRS 1915+105) have formed with kicks in excess of 50 km s^{-1} (see Table 7 for actual estimates and their associated errors).

At this point, we prefer to stay agnostic, allowing for both natal kick models: independent of BH mass and decreasing with BH mass. Further precise determinations of BH masses and BH natal kicks, are in our opinion needed to either support or reject claims that natal kicks decrease with BH mass.

6.10. Natal Kick Physical Mechanisms

Neutron star and black hole binaries can receive peculiar velocities in systems where the compact object forms in a supernova explosion with associated symmetric mass ejection. The binary system moves in the opposite direction of the ejecta (Blaauw 1961). This mechanism is not sufficient

to explain the observed pulsar velocity distribution and a number of additional "natal kick" mechanisms have been proposed to explain the proper motions of NSs. These kick mechanisms have implications for BH natal kicks and we will review them here. Natal kicks occur when there are asymmetries in either the matter ejected or the neutrinos emitted during the core collapse and/or supernova explosion. The velocity of the newly formed compact object is determined by the momentum conservation.

Normal supernovae are believed to be driven by the convection-enhanced engine where convection between the proto-NS and the edge of the stalled shock plays an important role in increasing the efficiency at which the gravitational potential energy is converted into energy driving an explosion. Both theoretical and observational evidence for this explosion engine as a mechanism behind normal supernovae has grown (for a review, see Fryer et al. 2014). Almost immediately after realizing that this convection could be important for the explosion, it was realized that low-mode convection could drive natal kicks (Herant 1995). Since this time, a series of calculations have been conducted to study the kicks from these convection cells (Scheck et al. 2006; Fryer & Young 2007). Although models have been constructed to obtain extremely high kicks, many models predict kicks in the 100–200 km s⁻¹ range. Alternatively, asymmetric ejecta can be driven by asymmetries in the density profile of collapsing core of a massive star (Burrows & Hayes 1996; Fryer 2004).

Although there is no decided ejecta kick mechanism, we can still make predictions for BH kicks assuming such mechanisms work. Momentum conservation sets the momentum of the BH (\mathbf{p}_{BH}) to be equal (but in opposite direction) to the momentum of the ejecta (\mathbf{p}_{ej}):

$$\mathbf{p}_{\text{BH}} = -\mathbf{p}_{\text{ej}}. \quad (23)$$

If the ejected material has a fixed asymmetry (α_{ej}), then the BH kick velocity (v_{BH}) is

$$v_{\text{BH}} = \frac{\alpha_{\text{ej}} M_{\text{ej}}}{M_{\text{BH}}} < v_{\text{ej}} > = \frac{\alpha_{\text{ej}} M_{\text{ej}}}{M_{\text{star}} - M_{\text{ej}}} < v_{\text{ej}} > \quad (24)$$

where M_{ej} is the ejecta mass, M_{BH} is the black hole mass, M_{star} is the mass of the star at collapse and $< v_{\text{ej}} >$ is the mass averaged velocity of the ejecta. In this formulation, if α_{ej} is constant, the kick velocity decreases with decreasing ejecta mass. Or to put it differently, asymmetric natal kick decreases with increasing BH mass. But, in the convective engine, the asymmetry in the explosion grows with time as the convection approaches lower modes. Late-time explosions are believed to be less energetic (with less ejecta and more massive BHs). In this scenario, the ejecta asymmetry increases with the explosion delay (and, hence, BH mass) and the BH kick can increase with increasing BH mass. Depending on the ejecta asymmetry behavior the magnitude of the natal kick may increase (fixed α_{ej}) or decrease (α_{ej} increasing with SN delay) with BH mass.

If the kick is instead produced by asymmetries in the pre-collapse stellar structure, the asymmetry is strongest at bounce and decreases with explosion delay. It means that the natal kick will decrease with increasing BH mass even faster than predicted by equation 24. Without understanding which asymmetry drives natal kick and without

knowledge of the evolution of the asymmetry with time, it is difficult to predict exact trends.

Asymmetries in the neutrino emission can be caused by a variety of mechanisms. Initial models focused on active (e, μ, τ) neutrinos, showing that these neutrinos can be produced with high asymmetries (Bisnovatyi-Kogan 1993; Lai & Qian 1998; Arras & Lai 1999; Kei, Shoichi & Katsuhiko 2005). Although these neutrinos can be produced with high asymmetries ($\sim 30\%$), by the time these neutrinos reach the neutrinosphere and escape, they are much more isotropic. If sterile neutrinos are produced, their immediate escape means that the escaping neutrinos are also asymmetric (Kusenko & Segre 1997; Nardi & Zuluaga 2001; Fuller et al. 2003; Kusenko 2005; Fryer & Kusenko 2006; Sagert & Schaffner-Bielich 2008; Kusenko 2009; Kisslinger, Henley & Johnson 2009; Kuznetsov & Mikheev 2012). For these sterile neutrinos, the magnitude of the kick depends also upon the fraction of energy converted into sterile neutrinos. Alternatively, neutrino asymmetries can be produced through radiatively-driven magnetoacoustic instabilities at the neutrinosphere (Socrates et al. 2005). Neutrino asymmetries can occur even without strong magnetic fields if asymmetric convection can induce asymmetries in the neutrino emission. The kick magnitudes from these asymmetries are typically low (for a review, see Janka 2013).

As with the ejecta kick mechanisms, it is difficult to estimate the natal kick dependence on BH mass without using a specific model. The collapse of a massive star releases a collapse energy:

$$E_{\text{coll}} = \frac{GM_{\text{NS}}^2}{r_{\text{NS}}} \approx 2.7 \times 10^{53} \left(\frac{M_{\text{NS}}}{M_{\odot}} \right)^2 \text{ erg}, \quad (25)$$

most of which is carried away by neutrinos (with a momentum of E_{coll}/c where c is the speed of light). If we assume the neutrino asymmetry is constant until the core collapses to a BH, the kick produced by asymmetric neutrino emission is:

$$v_{\text{BH}} = 150 \frac{\alpha_{\nu}}{0.01} \frac{3 M_{\odot}}{M_{\text{BH}}} \frac{E_{\text{coll}}}{2.7 \times 10^{53} \text{ erg}} \quad (26)$$

where α_{ν} is the asymmetry in the neutrinos. This relation generates natal kicks that decrease with BH mass. However, it also indicates that even massive BHs may receive significant natal kicks. For example, if we assume that the maximum NS mass is $2.2 M_{\odot}$, the average asymmetry of the neutrinos is 1%, a BH of mass $10 M_{\odot}$ could receive a kick in excess of 200 km s⁻¹.

If the stellar core is not rotating rapidly, the neutrino emission will drop dramatically after the neutron star collapses to a black hole. Any neutrino kick mechanism will shut down at the formation of the black hole (this is assumed in our estimate of the available collapse energy; eq. 25). Even if the magnetic field grows with time, producing a stronger neutrino asymmetry with time, this turn-off will likely produce weaker kicks for more massive black holes. However, if the core is rotating rapidly, neutrino emission from the black hole accretion disk can dominate the total neutrino budget (e.g., neutrinos from collapsar model: Popham, Woosley & Fryer 1999; Fryer & Meszaros 2003). If some mechanism can be devised to

produce asymmetric emission from this disk (e.g. instabilities similar to those discussed by Socrates et al. 2005), the BH kick could grow with increasing black hole mass.

Unfortunately, both the ejecta and neutrino mechanisms predict the same trends in general: more massive black holes will have lower kicks. There are some differences. Most of the neutrino mechanisms argue for kicks aligned with the spin axis and this need not be the case for the ejecta mechanisms (although, the ejecta velocity is likely to be aligned with the spin axis in rapidly rotating systems). In neutrino mechanisms, the kick need not be directed in the opposite direction of the ejecta. Indeed, for some mechanisms, the ejecta and kick can be in the same direction (Fryer & Kusenko 2006). Finally, the neutrino-driven kick mechanism can occur even if there is no supernova explosion (no mass loss/ejecta) at all. Although measurements of natal kicks and their dependence on BH mass may not point unambiguously to a particular kick mechanism, they could provide very useful information on development of asymmetry in core collapse/supernova explosion. Whether the asymmetry comes in the form of mass ejection or neutrino emission, such measurements would allow to constrain and improve supernova models.

7. POTENTIAL REDUCTION OF BH-BH MERGER RATES

In case of the non-detection of massive BH-BH mergers, high black hole natal kicks (as we argue throughout this study) are one of two current proposals for how to limit their formation. Mennekens & Vanbeveren (2014) find no BH-BH mergers in their population synthesis predictions. This finding applies to BH-BH mergers of any mass and it is connected with very intensive stellar wind mass loss. Intensive mass loss not only decreases the amount of mass available for BH formation, but also limits the radial evolution of a star. The expansion is required at late evolutionary stages to lead to RLOF that needs to develop into CE, allowing for orbital contraction and the formation of a coalescing BH-BH binary. Mennekens & Vanbeveren (2014) claim that the mass loss for BH progenitors may be so intensive (especially during the LBV phase) that it bars BH-BH formation.

In general, the radial expansion of massive stars is not fully understood. Radial expansion may be limited on the outside by strong stellar winds removing the H-rich envelope, and on the inside by mixing envelope H-rich material into the core (either by strong convection and/or by rapid rotation).

At high metallicity (strong stellar winds) it is claimed that massive stars above $M_{\text{zams}} > 40 M_{\odot}$ do not significantly expand as they are not observed in specific parts of the H-R diagram (e.g., Mennekens & Vanbeveren 2014). However, stars with somewhat lower mass $\sim 20\text{--}40 M_{\odot}$ are observed to expand to large radii (AH Sco: $1400 R_{\odot}$, UY Sct: $1700 R_{\odot}$, KW Sgr: $1000 R_{\odot}$) in the Milky Way, so at rather high metallicity (Arroyo-Torres et al. 2013).

At low metallicity (i.e. 10% solar, at and below which we predict effective close BH-BH formation) there is no available observational information on the radii of massive stars. Evolutionary models show that already at SMC metallicity (20–30% solar) stars up to $60 M_{\odot}$ expand to

large radii and become red super giants (Brott et al. 2011).

Although the mass range for BH formation is not well constrained, with claims that change from a lower limit for BH formation of $M_{\text{zams}} > 20 M_{\odot}$ (e.g., Dominik et al. 2014) to $M_{\text{zams}} > 40 M_{\odot}$ (e.g., Mennekens & Vanbeveren 2014) to no limit at all with NS/BH formation being a rather chaotic function of initial star mass (Clausen, Piro & Ott 2015) there seems to be still a lot of parameter space available for radial expansion of potential BH progenitors.

Stellar winds tend to increase orbital separation between two massive stars in a binary system. If wind mass loss is large (as expected for massive stars) and if stars do not expand significantly, binary components may never reach RLOF/CE. Tidal interactions may be a potential mediating factor. If a massive star expands after main sequence it slows down, if it is not already a slow rotator. If a star radius reaches about half the size of its Roche lobe the tides will tend to spin the star up at the expense of the binary angular momentum. This effect may be stronger than the increase of orbital separation due to wind mass loss. The orbit decreases and the star may initiate RLOF/CE. Such a case was demonstrated for a $40 M_{\odot}$ star with the extreme LBV mass loss adopted from Mennekens & Vanbeveren (2014). This star was placed in a binary with a $7 M_{\odot}$ black hole, and the binary was shown to form a typical BH-BH merger despite the intense wind mass loss rate (Dominik et al. 2015). On the other hand, it is unclear how effectively tides dissipate energy. If tidal energy dissipation is not very effective the orbital contraction (and thus RLOF/CE) is not expected unless a star does not expand much on its own, as in such a case strong winds dominate the evolution of binary separation. Tidal interactions in close binary systems are not taken into account in the evolutionary model of Mennekens & Vanbeveren (2014), so they have not considered the effects of this mitigating factor on their no BH-BH merger proposal.

8. NS-NS MERGER RATES

Our predicted rate densities for NS-NS mergers for advanced LIGO/Virgo are presented in Figures 5 and 6 and Tables 5 and 6 (the first mass bin). These merger rate densities, although low ($\sim 0.5\text{--}1.7 \times 10^{-7} \text{ Mpc}^{-3} \text{ yr}^{-1}$), are consistent with available empirical estimates.

Kim et al. (2010) have estimated NS-NS merger rate based on observations of three Galactic field NS-NS systems, B1913+16, B1534+12, and J0737-3039, and found a Galactic merger rate within the range $3\text{--}190 \text{ Myr}^{-1}$. O’Shaughnessy & Kim (2010) obtained a median value of 89 Myr^{-1} , with a spread above and below by a factor of ~ 3 when pulsar beaming constraints are taken into account. Kim, Perera & McLaughlin (2015) have re-examined the influence of double pulsar J0737-3039³, obtaining a revised estimate of the Galactic merger rate of $7\text{--}49 \text{ Myr}^{-1}$, with median value 21 Myr^{-1} . These headline numbers do not include the large uncertainties in the pulsar luminosity function. If these uncertainties are included, it is expected that the rates could shift up or down by an order of magnitude (Kalogera et al. 2004; Mandel & O’Shaughnessy 2010; Abadie et al. 2010). Applying this to the most recent estimate results in a broad range

³Note that it’s not the double pulsar that decreases the previous rate estimates

⁴These rates are obtained with the assumption of Galactic 10 Gyr of constant star formation rate at the level $3.5 M_{\odot} \text{ yr}^{-1}$.

of allowed rates: 2.1–210 Myr⁻¹.

For comparison, the Galactic merger rates⁴ in our standard and optimistic evolutionary scenario are 7.6 and 23.5 Myr⁻¹, respectively. Note that these *Galactic* rates are not listed separately in any of our tables, but are used for all the predictions, contributing a part of the over-all NS-NS merger rate (which results from galaxies of various metallicities). The actual Galactic merger rates (that are used here) are reported in Dominik et al. 2012; see their Table 2 for $Z = 0.02$). These rates are relevant for Galactic field evolution where the majority of NS-NS binaries are found. Our NS-NS merger rates for sub-solar metallicity ($Z = 0.002$; Table 3 of Dominik et al. 2012) are a factor of ~ 3 lower. The full spread of NS-NS Galactic rates for the solar metallicity models is 23.3–77.4 Myr⁻¹ for the Dominik et al. (2012) A submodels (they correspond to our optimistic assumption on CE) and 0.3–9.5 Myr⁻¹ for the B submodels (our standard model assumption on CE). The predicted NS-NS merger rates are fully consistent with Galactic NS-NS observations for our optimistic model (V1), and are on the lower end of empirical estimates for our other models (V2, V3, V4). In particular, our simple estimate is consistent with the detailed analysis of pulsar luminosity function uncertainty by O’Shaughnessy & Kim (2010; see their Fig 11).

There is mounting evidence that short Gamma-ray bursts (GRBs) are connected with NS-NS and/or BH-NS mergers (e.g., Berger 2013), and some authors have used short GRB rates to estimate NS-NS merger rates (e.g., Chen & Holz 2013). Fong et al. (2012) found short GRB rate densities at the level 100–1,000 Gpc⁻³ yr⁻¹, while Enrico Petrillo, Dietz, & Cavagila (2013) estimated the rate density to be 500–1,500 Gpc⁻³ yr⁻¹. These results suffer from short GRB beaming and luminosity uncertainties. The beaming has been firmly established for ~ 3 short GRBs (with $\theta_j \lesssim 10$ deg), while redshifts and thus luminosities are only known for the ~ 20 closest events. It is possible that the average beaming angle is larger than currently estimated, and that the rates densities are correspondingly lower, possibly by an order of magnitude (E.Berger 2013, private communication). The lower limit on the short GRB rate density would then decrease to 10 Gpc⁻³ yr⁻¹. Before comparing with our NS-NS merger rate density it is worth noting that even if NS-NS mergers are in fact short GRB progenitors, they may be responsible for only a fraction of short GRBs as other progenitors cannot be excluded at the moment (e.g., Nakar 2010). On the other hand only some fraction of NS-NS mergers may produce short GRBs (e.g., Fryer et al. 2015). The NS-NS merger rate densities that we report here (tables and figures) are at the level of 50–150 Gpc⁻³ yr⁻¹. We note that our reported merger rate densities apply *only* to the local Universe within the reach of advanced LIGO/Virgo for NS-NS mergers (450 Mpc; $z < 0.1$). Our NS-NS merger rate densities are predicted to moderately increase with redshift at low redshifts (see Fig. 3 in Dominik et al. 2013). Considering all of the above, our reported NS-NS merger rate densities are only a lower limit on the overall GRB rate density, and thus they are consistent with GRB rate predictions.

9. CONCLUSIONS

(I) *Executive summary.* We performed a comparison of evolutionary predictions for NS-NS, BH-NS, and BH-BH mergers with observational upper limits for gravitational wave detectors. We note that, due to cosmological and evolutionary effects, some care must be taken in the process of making these comparisons. In particular, in the case of advanced LIGO/Virgo detectors with their significant detection horizon (reaching redshift of $z = 2$ for BH-BH mergers), a careful analysis of evolutionary and population synthesis predictions is required.

Our conclusions and results are based on theoretical evolutionary calculations of Dominik et al. (2012, 2013, 2015) and are available online; <http://www.syntheticuniverse.org>. We find that the most likely sources to be detected with the advanced detectors are massive BH-BH mergers with total redshifted mass ~ 30 –70 M_\odot , consisting of almost equal mass black holes with aligned spins.

This major finding is supported by the revised estimate for the stellar-origin maximum mass BH: 80 M_\odot for stars below initial mass of 150 M_\odot (Belczynski et al. 2010). Further, there is observational evidence that supports the existence of massive BH-BH binaries with short coalescence times. Bulik, Belczynski & Prestwich (2011) argued that the two massive extragalactic binaries IC10 X-1 and NGC300 X-1 are immediate progenitors of massive BH-BH mergers with intrinsic chirp mass in the range ~ 10 –30 M_\odot (total intrinsic merger mass of ~ 25 –70 M_\odot for equal mass black holes). The estimated empirical detection rate was so high that it was calculated that these BH-BH mergers could have been detected in LIGO/Virgo initial observations. The failure to detect such binaries in S5/S6 LIGO/Virgo observations may be attributed to a potential overestimate of binary component masses in IC10 X-1 and NGC300 X-1. The mass determinations for these two binaries are subject to large uncertainty, as originally introduced and described by van Kerkwijk et al. (1996; see also our brief description of this issue in Sec. 6.8).

The above conclusion is derived from a majority of our models and is based on our estimates and arguments for the best input stellar and binary physics. However, we have attempted to convey that the large uncertainties involved in evolutionary predictions do not allow us to make absolute predictions in favor of or against detections. We point out that the possibility remains that no BH-BH mergers will be detected even with the full sensitivity of advanced LIGO/Virgo (see below).

(II) *BH natal kicks and field/cluster massive BH-BH mergers.* In Sections 6.1 to 6.9 we argued that current electromagnetic constraints can not separate two basic trends: (1) natal kicks decrease with BH mass and (2) natal kicks are independent of BH mass. In Section 6.10 we argued that both basic natal kick mechanisms: (i) asymmetric mass ejection and (ii) asymmetric neutrino emission may have very similar signatures. For example, both of these mechanisms may generate natal kicks decreasing with BH mass, or both mechanisms may generate significant (in excess of 200 km s⁻¹) natal kicks for massive ($> 10 M_\odot$) BHs. This means that even if observations (whether electromagnetic or in gravitational radiation) will constrain the natal kick dependence on BH mass, the true physical mechanism generating the kicks may still

remain a mystery. The only exception would be the case in which the natal kick increases with BH mass, as such the trend would be consistent *only* with the asymmetric mass ejection mechanism in which asymmetry of ejecta grows with supernova delay time. Even if BH natal kick mechanism is not recognized, the measurement of the natal kick dependence on BH mass may provide very useful information for core collapse/supernova modeling.

We have demonstrated in Section 5 that the two basic trends in the natal kick dependence on BH mass lead to very different predictions for BH-BH mergers. For natal kicks decreasing with BH mass, our standard evolutionary model predicts abundant detections of massive BH-BH mergers (with total redshifted mass $\sim 30\text{--}70 M_{\odot}$) by advanced LIGO/Virgo. For natal kicks independent of BH mass our model with high kicks predicts that BH-BH merger detections are unlikely with advanced LIGO/Virgo. Finally, advanced LIGO/Virgo detections or non-detections of massive BH-BH mergers may constrain BH natal kicks, but they are unlikely to provide information on the physical mechanism producing the natal kick.

Frequent detections of the massive BH-BH mergers will be indication that BHs receive low (if any) natal kicks. We have shown that high BH kicks severely limit LIGO/Virgo detections of BH-BH mergers originating from isolated (field) binary evolution (see Sec. 5). In addition, although recent results show efficient BH-BH merger formation in globular clusters (Morscher et al. 20015; Rodriguez et al. 2015), the majority of these systems would similarly be disrupted if there are high BH kicks (M.Morscher, 2015: Aspen Black Holes in Dense Star Clusters conference communication).

In the case of low BH natal kicks (at least for massive BHs), abundant mergers are expected both from evolution of the field population (~ 500 detections per year; Dominik et al. (2015) standard input physics result) and from globular cluster evolution (~ 100 detections per year; Rodriguez et al. (2015) typical estimate). Field massive BH-BH mergers are predicted to reach intrinsic (not redshifted) chirp mass of $50 M_{\odot}$ (total intrinsic merger mass of $\sim 120 M_{\odot}$ for equal mass black holes), have almost equal mass components and aligned spins. Our model with low BH natal kicks (natal kicks decreasing with BH mass) employs no mass ejection and no natal kicks for massive BHs, and therefore it naturally produces massive BH-BH mergers with aligned spins. Cluster massive BH-BH mergers are predicted to reach intrinsic chirp mass of $30 M_{\odot}$ (total intrinsic merger mass of $\sim 70 M_{\odot}$ for equal mass black holes), have almost equal mass components (C.Rodriguez, private communication 2015) and misaligned spins. The misalignment is expected due to the dynamical captures/exchanges involved in the formation of BH-BH binaries and also due to the tilting of orbits during the dynamical encounters in dense star clusters. In the case of abundant detections, extracting spin information from the binaries would provide a powerful probe of the origin of the binary systems.

(III) *BH-BH non-detection case.* In the case of non-detection of massive BH-BH mergers by advanced LIGO/Virgo, it may not be clear which physical process

is most responsible for limiting BH-BH binary formation. Two suppression mechanisms have been identified and discussed (see Sec. 7): high BH natal kicks (this study) and strong stellar winds (Mennekens & Vanbeveren 2014). However, it is worth noting that strong winds should not affect dynamically formed BH-BH mergers. Therefore detections with confirmed cluster origin combined with non-detection from field populations would in principle clarify this issue. Of course, other inhibitory processes may also exist.

(IV) *Very massive stellar origin BH-BH mergers.* The above considerations apply only to the evolution of stars with initial mass below $150 M_{\odot}$. Recent observations of the R136 cluster in the LMC ($\sim 0.6 Z_{\odot}$) identified stars with masses larger than $150 M_{\odot}$ (Crowther et al. 2010). This may be an indication that the IMF extends to much higher masses that were considered previously *only* for primordial (Population III) stars in the high redshift Universe. If this is the case, there may exist an additional population of very massive stellar origin BHs with mass $\gtrsim 100 M_{\odot}$ (Yusof et al. 2013). Formation of close BH-BH systems from these massive stars may be possible, although estimates are subject to severe uncertainties. If detections of such objects are made, they will provide information on the extent of the IMF and the occurrence of pair instability supernovae (Belczynski et al. 2014).

We would like to thank a number of colleagues who helped us to improve our project over past several years. We want to name not only those who have given us information and positive feedback, but also many of these who gave us critique and who disagreed with us. The full list includes Ilya Mandel, Gijs Nelemans, Selma de Mink, Felix Mirabel, Tsvi Piran, Patric Brady, Alessandra Buonanno, David Reitze, Vicky Kalogera, Tassos Fragos, Megan Morscher, Carl Rodriguez, Tom Maccarone and Dany Vanbeveren. KB and MD acknowledge support from the NCN grant Sonata Bis 2 (DEC-2012/07/E/ST9/01360) and FNP professorial subsidy MASTER 2013. TB and KB acknowledge support from the NCN grant Harmonia 6 (UMO-2014/14/M/ST9/00707). This work was supported in part by National Science Foundation Grant No. PHYS-1066293 and the hospitality of the Aspen Center for Physics (KB, DH). This work was partially supported by a grant from the Simons Foundation (KB). ROS was supported by NSF grant PHY-1505629. DEH was supported by NSF CAREER grant PHY-1151836. He also acknowledges support from the Kavli Institute for Cosmological Physics at the University of Chicago through NSF grant PHY-1125897 as well as an endowment from the Kavli Foundation. EB is supported by NSF CAREER grant PHY-1055103 and by FCT Contract IF/00797/2014/CP1214/CT0012 under the IF2014 Programme. The work of CF was done under the auspices of the National Nuclear Security Administration of the U.S. Department of Energy, and supported by its contract DEAC52-06NA25396 at Los Alamos National Laboratory. TB was supported by the NCN grant UMO-2014/15/Z/ST9/00038.

- Aasi, J., et al. 2013a, *Phys. Rev. D.*, 87, 022002
Aasi, J., et al. 2013b, arXiv:1304.0670
Aasi, J., et al. 2014a, *Phys. Rev. D*, 89, 102006
Aasi, J., et al. 2014b, *Phys. Rev. D*, 89, 122003
Abadie, J., et al. 2010, *CQG*, 27, 173001
Abadie, J., et al. 2012, *Phys. Rev. D*, 85, 082002
Abadie, J., et al. 2015, *CQG*, 32, 074001
Abbott, B., et al. 2009, *Rept. Prog. Phys.*, 72, 076901
Accadia, T., et al. 2012, *Journal of Instrumentation*, 7, 3012
Acerese et al. 2015, *CQG*, 32, 024001
Ajith, P., Bose, S. 2009, *Phys. Rev. D*, 79, 084032
Ajith, P. 2011, *Phys. Rev. D*, 84, 084037
Arras, P., Lai, D. 1999, *ApJ*, 519, 745
Arroyo-Torres, B., Wittkowski, M., Marcaide, J., & Hauschildt, P. 2013, *A&A*, 554, 76
Asplund M., Grevesse, N., Sauval, A., Scott, P. 2009, *ARA&A*, 47, 481
Bailyn, C., Jain, R., Coppi, P., & Orosz, J. 1998, *ApJ*, 499, 367
Beer, M., Podsiadlowski, P. 2002, *MNRAS*, 331, 351
Belczynski, K., Bulik, T. 2002, *ApJ*, 574, L147
Belczynski, K., Kalogera, V., Bulik, T. 2002, *ApJ*, 572, 407
Belczynski, K., et al. 2007, *ApJ*, 662, 504
Belczynski, K., et al. 2008, *ApJS*, 174, 223
Belczynski, K., et al. 2010a, *ApJ*, 715, L138
Belczynski, K., et al. 2010b, *ApJ*, 714, 1217
Belczynski, K., Wiktorowicz, G., Fryer, C., Holz, D., & Kalogera, V. 2012, *ApJ*, 757, 91
Belczynski, K., Buonanno, A., Cantiello, M., Fryer, C., Holz, D., Mandel, I., Miller, & C., Walczak, M. 2014, *ApJ*, 789, 120
Berger, E., Fong, W., Chornock, R. 2013, *ApJ*, 774, L23
Berger, E. 2013, *ARA&A*, 52, 43
Bisnovatyi-Kogan, G. 1993, *A&AT*, 3, 287
Blaauw, A. 1961, *Bull. Astron. Inst. Netherlands*, 15, 265
Brandt, N., Podsiadlowski, P. 1995, *MNRAS*, 274, 461
Brott, I., de Mink, S., Cantiello, M., Langer, N., de Koter, A., Evans, C., Hunter, I., Trundle, C., & Vink, J. 2011, *A&A*, 530, 115
Bulik, T., Belczynski, K., Prestwich, A. 2011, *ApJ*, 730, 140
Burrows, A., Hayes, J. 1996, *Phys. Rev. Lett.*, 76, 352
Cantrell, J., et al. 2010, *ApJ*, 710, 1127
Chen, H.-Y., Holz, D.E. 2013, *Phys. Rev. Lett.*, 111, 181101
Clausen, D., Piro, A., & Ott, C. 2015, *ApJ*, 799, 190
Crowther, P., Schnurr, O., Hirschi, R., Yusof, N., Parker, R., Goodwin, S., & Kassim, H. 2010, *MNRAS*, 408, 731
de Mink, S., & Belczynski, K. 2015, *ApJ*, accepted (arXiv:1506.03573)
Dhawan, V., Mirabel, F., Ribo, M., Rodrigues, I. 2007, *ApJ*, 668, 430
Dominik, M., Belczynski, K., Fryer, C., Holz, D., Berti, E., Bulik, T., Mandel, I., & O'Shaughnessy, R. 2012, *ApJ*, 759, 52
Dominik, M., Belczynski, K., Fryer, C., Holz, D., Berti, E., Bulik, T., Mandel, I., & O'Shaughnessy, R. 2013, *ApJ*, 779, 72
Dominik, M., Berti, E., O'Shaughnessy, R., Mandel, I., Belczynski, K., Fryer, C., Holz, D., Bulik, T., & Pannarale, F. 2015, *ApJ*, 806, 263
Einstein, A. 1918, *Über Gravitationswellen*, *Sitzungsberichte der physikalisch-mathematischen Klasse*, 1, 154
Enrico Petrillo, C., Dietz, A., & Cavagila, M. 2013, *ApJ*, 767, 140
Filippenko, A., Matheson, T., Leonard, D., Barth, A., van Dyk, S. 1997, *PASP*, 109, 461
Filippenko, A., Leonard, D., Matheson, T., Li, W., Moran, E., Riess, A. 1999, *PASP*, 111, 969
Finn, L., & Chernoff, D. 1993, *Phys. Rev. D*, 47, 2198
Fong, W., et al. 2012, *ApJ*, 756, 189
Fragos, T., Willems, B., Kalogera, V., Ivanova, N., Rockefeller, G., Fryer, C.L., Benz, W., Herant, M., Colgate, S. 1999, *ApJ*, 516, 892
Fryer, C.L., Meszaros, P. 2003, *ApJ*, 588, L25
Fryer, C.L., et al. 2004, *ApJ*, 601, L175
Fryer, C.L., Kusenko, A. 2006, *ApJS*, 163, 335
Fryer, C.L., Young, P. 2007, *ApJ*, 659, 1438
Fryer, C.L., et al. 2012, *ApJ*, 749, 91
Fryer, C.L., Even, W., Grefenstette, B., Wong, T. 2014, *AIP Advances*, 4, 041014
Fryer, C.L., Belczynski, K., Ramirez-Ruiz, E., Rosswog, S., Shen, G., Steiner, A. 2015, *ApJ*, 812, 24
Fuller, G., Kusenko, A., Mocioiu, I., Pascoli, S. 2003, *Phys. Rev. D*, 68, 103002
Garcia, B., Mermilliod, J. 2001, *A&A*, 368, 122
Gelino, D., Harrison, T., & McNamara, B. 2001, *ApJ*, 122, 971
Gelino, D., Harrison, T. 2003, *ApJ*, 599, 1254
Gonzalez Hernandez, J., Rebolo, R., Israelian, G., Harlaftis, E., Filippenko, A., Chornock, R. 2006, *ApJ*, 644, L49
Gonzalez Hernandez, J., Rebolo, R., Israelian, G., Filippenko, A., Chornock, R., Tominaga, N., Umeda, H., Nomoto, K. 2008, *ApJ*, 679, 732
Greiner, J., Cuby, J., & McCaughrean, M. 2001, *Nature*, 414, 522
Harlaftis, E., et al. 1997, *AJ*, 114, 1170
Harris, W. 1996, *AJ*, 112, 1487
Harry G., et al. 2010, *CQG* 27, 084006
Herant, M. 1995, *Phys. Reports*, 256, 117
Hobbs, G., Lorimer, D. R., Lyne, A. G., & Kramer, M. 2005, *MNRAS*, 360, 974
Hurley, D., Callanan, P., Elebert, P., Reynolds, M. 2013, *MNRAS*, 430, 1832
Ioannou, Z., Robinson, E., Welsh, F., & Haswell, C. 2004, *AJ*, 127, 481
Israelian, G., Rebolo, R., Basri, G., Casares, J., Martin, E. 1999, *Nature*, 401, 142
Ivanova, N., Belczynski, K., Kalogera, V., Rasio, F., Taam, R. 2003, *ApJ*, 592, 475
Ivanova, N., et al. 2013, *A&ARv*, 21, 59
Janka, T. 2013, *MNRAS*, 434, 1355
Juric, M., et al. 2008, *ApJ*, 673, 864
Justham, S., Rappaport, S., Podsiadlowski, P. 2006, *MNRAS*, 366, 1415
Kalogera et al. 2004, *ApJ*, 601, L179; erratum *ibid.* 614, L137
Kei, K., Shoichi, Y., Katsuhiko, S. 2005, *ApJ*, 618, 474
Khargharia, J., Froning, C., Robinson, E. 2010, *ApJ*, 716, 1105
Khargharia, J., Froning, C., Robinson, E., & Gelino, D. 2013, *AJ*, 145, 21
Kim, C., Kalogera, V., Lorimer, D. 2010, *New Astr. Rev.*, 54, 148
Kim, C., Perera, B., McLaughlin, M. 2015, *MNRAS*, 448, 928
Kiminki, D., Kobulnicky, H., Kinemuchi, K., Irwin, J., Fryer, C., Berrington, R., Uzpen, B., Monson, A., Pierce, M., Woosley, S. 2007, *ApJ*, 664, 1102
Kisslinger, L., Henley, E., Johnson, M. 2009, *Modern Physics Lett. A*, 24, 2507
Kobulnicky, H., Fryer, C. 2007, *ApJ*, 670, 747
Kobulnicky, H., et al. 2014, *ApJS*, 213, 34
Kopparapu, R. K., Hanna, C., Kalogera, V., et al. 2008, *ApJ*, 675, 1459
Kreidberg, L., Bailyn, C., Farr, W., & Kalogera, V. 2012, *ApJ*, 757, 36
Kusenko, A. 2005, *IJMPA*, 20, 1148
Kusenko, A. 2009, *Physics Reports*, 481, 1
Kusenko, A., Segre, G. 1997, *Physics Lett. B*, 396, 197
Kuznetsov, A., Mikheev, N. 2012, *Astronomy Letters*, 38, 436
Lai, D. 2001, in *Physics of Neutron Star Interiors*, ed. by D. Blaschke, N.K. Glendenning and A. Sedrakian, *Lecture Notes in Physics*, vol. 578, p.424
Lai, D., Qian, Y. 1998, *ApJ*, 505, 844
Lattimer, J., & Prakash, M. 2011, in *Gerry Brown's Festschrift*, and in *From Nuclei to Stars*, ed. S. Lee, p.275.: Singapore, World Scientific (arXiv:1012.3208)
Li, Z., Qu, J., Song, L., Ding, G., & Zhang, C. 2013, *MNRAS*, 428, 1704
Macias, P., et al. 2011, in *Bulletin of the American Astronomical Society*, Vol. 43, 143.04
Madau, P., & Dickinson, M. 2014, *ARA&A*, 54, 415
Mandel, I. & O'Shaughnessy, R. 2010, *CQG*, 27, 114007
Martin, A., Casares, J., Charles, P., van der Hooft, F., van Paradijs, J. 1995, *MNRAS*, 274, L46
Mennekens, N., & Vanbeveren, D. 2014, *A&A*, 564, 134
Meurs, E. & van den Heuvel, E. 1989, *A&A*, 226, 88
Miller-Jones, J., Jonker, P., Dhawan, V., Briskin, W., Rupen, M., Nelemans, G., Gallo, E. 2009a, *ApJ*, 706, L230
Miller-Jones, J., Jonker, P., Nelemans, G., Portegies-Zwart, S., Dhawan, V., Briskin, W., Gallo, E., Rupen, M. 2009b, *MNRAS*, 394, 1440
Mirabel, F., & Rodrigues, I. 2003, *Science*, 300, 1119
Morscher, M., Pattabiraman, B., Rodriguez, C., Rasio, F., & Umbreit, S. 2015, *ApJ*, 800, 9
Motta, S., Belloni, T., Stella, L., Muoz-Darias, T., Fender, R. 2014, *MNRAS*, 437, 2554
Nakar, E. 2010, proceedings of the The Shocking Universe Venice meeting (arXiv:1009.4648)
Nardi, E., Zuluaga, J. 2001, *ApJ*, 549, 1076
Orosz, J., Jain, R., Bailyn, C., McClintock, J., & Remillard, R. 1998, *ApJ*, 499, 375
Orosz, J., Kuulkers E., van der Klis M., McClintock J., Garcia M., Callanan P., Bailyn C., Jain R., Remillard R. 2001, *ApJ*, 555, 489
Orosz, J., McClintock, J., Aufdenberg, J., Remillard, R., Reid, M., Narayan, R., & Gou, L. 2011, *ApJ*, 742, 84
O'Shaughnessy, R., Kim, C. 2010, *ApJ*, 715, 230
Pan, Y., Buonanno, A., Boyle, M., Buchman, L., Kidder, L., Pfeiffer, H., Scheel, M. 2011, *Phys. Rev. D*, 84, 124052
Pannarale, F., Berti, E., Kyutoku, K., & Shibata, M. 2013, *Phys. Rev. D*, 88, 084011
Panter, B., Jimenez, R., Heavens, A., & Charlot, S. 2008, *MNRAS*, 391, 1117
Peters, P., & Mathews, J. 1963, *Phys. Rev.*, 131, 435
Popham, R., Woosley, S., Fryer, C.L. 1999, *ApJ*, 518, 356
Prestwich, A., et al. 2007, *ApJ*, 669, L21

- Reid, M., et al. 2011, *ApJ*, 742, 83
 Reid, M., et al. 2014, *ApJ*, 796, 2
 Repetto, S., Davies, M., & Sigurdsson, S. 2012, *MNRAS*, 425, 2799
 Repetto, S., Nelemans, G. 2015, *MNRAS*, 453, 3341
 Reynolds, M., Callanan, P., & Filippenko, A. 2007, *MNRAS*, 374, 657
 Rodriguez, C., Morscher, M., Pattabiraman, B., Chatterjee, S., Haster, C., Rasio, F. 2015, *Phys. Rev. Lett.* 115, 051101
 Sagert, I., Schaffner-Bielich, J. 2008, *Journal of Physics G: Nuclear and Particle Physics*, 35, 014062
 Sana, H. et al. 2012, *Science*, 337, 444
 Santamaria, L., Ohme, F., Ajith, P., et al. 2010, *Phys.Rev.D*, 82, 064016
 Sathyaprakash, B., Schutz, B. 2009, *Living Rev. Relativity*, 12, 2
 Scheck, L., Kifonidis, K., Janka, T., Muller, E. 2006, *A&A*, 457, 963
 Sepinsky, J., Willems, B., Kalogera, V., Rasio, F. 2010, *ApJ*, 724, 546
 Shoemaker, D. for the LIGO Scientific Collaboration. 2010, *Advanced LIGO anticipated sensitivity curves*, <https://dcc.ligo.org/LIGO-T0900288/public>
 Silverman, J., & Filippenko, A., 2008, *ApJ*, 678, L17
 Socrates, A., Blaes, O., Hungerford, A., Fryer, C.L. 2005, *ApJ*, 632, 531
 Steeghs, D., et al. 2013, *ApJ*, 768, 185
 Stevenson, S., Ohme, F., & Fairhurst, S. 2015, *ApJ*, 810, 58
 Tanvir, N., et al. 2013, *Nature*, 500, 547
 Tauris, T., & Takens, R. 1998, *A&A*, 330, 1047
 van Kerkwijk, M., Geballe, T., King, D., van der Kils, M., & van Paradijs, J. 1996, *A&A*, 314, 521
 Villante, F., Serenelli, A., Delahaye, F., Pinsonneault, M. 2014, *ApJ*, 787, 13
 Vink, J.S., de Koter, A., & Lamers, H. 2001, *A&A*, 369, 574
 Webbink, R. 1984, *ApJ*, 277, 355
 Weisberg, J., & Taylor, J. 2005, in *Binary Radio Pulsars*, ASP Conference Series, Vol. 328, Edited by F. A. Rasio and I. H. Stairs. San Francisco: Astronomical Society of the Pacific, p.25
 Wiktorowicz, G., Belczynski, K., Maccarone, T. 2014, *arXiv:1312.5924*
 Willems, B., Henninger, M., Levin, T., Ivanova, N., Kalogera, V., McGhee, K., Timmes, F.X., & Fryer, C.L. 2005, *ApJ*, 625, 324
 Wong, T.-W., Valsecchi, F., Fragos, T., & Kalogera, V. 2012, *ApJ*, 747, 111
 Wong, T.-W., Valsecchi, F., Ansari, A., Fragos, T., Glebbeek, E., Kalogera, V., & McClintok, J. 2014, *ApJ*, 790, 119
 Xu, X., & Li, X. 2010, *ApJ*, 716, 114
 Yusof, N., Hirschi, R., Meynet, G., Crowther, P., Ekstrom, S., Frischknecht, U., Georgy, C., Abu Kassim, H., Schnurr, O. 2013, *MNRAS*, 433, 1114

TABLE 1
 MERGER RATE DENSITY CALCULATION METHODS [$\text{MPC}^{-3} \text{YR}^{-1}$] ^a

$M_{\text{tot},z}/ M_{\odot}$ ^b	aLIGO ^c	Methods		
		I (V2)	II (V2l)	III (V2l)
2-5	1.2e-07	6.0e-08	5.7e-08	5.7e-08
5-8	3.3e-08	2.5e-10	3.0e-11	1.2e-11
8-11	1.6e-08	5.1e-09	1.7e-09	8.7e-10
11-14	1.0e-08	1.0e-08	1.2e-09	2.1e-09
14-17	6.7e-09	2.5e-08	6.4e-09	2.4e-09
17-20	4.9e-09	5.4e-09	8.9e-09	6.9e-09
20-25	3.6e-09	1.8e-08	3.8e-09	6.9e-09
25-37	2.2e-09	2.5e-08	1.1e-08	6.5e-09
37-54	1.2e-09	1.6e-09	1.5e-08	1.5e-08
54-73	7.7e-10	0.0	4.9e-09	6.0e-09
73-91	5.6e-10	0.0	1.7e-09	4.9e-09
91-109	4.3e-10	0.0	4.5e-10	1.1e-09
109-127	3.5e-10	0.0	2.7e-10	4.2e-10
127-145	2.9e-10	0.0	2.1e-10	3.0e-10
145-163	2.5e-10	0.0	8.8e-11	1.9e-10
163-181	2.2e-10	0.0	7.8e-11	1.7e-10
181-199	2.0e-10	0.0	6.8e-11	1.8e-10
199-217	1.8e-10	0.0	4.7e-11	1.7e-10
217-235	1.6e-10	0.0	3.0e-11	1.3e-10
235-253	1.5e-10	0.0	7.9e-12	6.1e-11
253-271	1.4e-10	0.0	4.8e-12	4.5e-11
271-289	1.3e-10	0.0	4.3e-12	2.3e-11
289-307	1.2e-10	0.0	3.1e-12	2.2e-11
307-325	1.1e-10	0.0	1.0e-12	6.9e-12
325-343	1.1e-10	0.0	6.6e-13	1.0e-11
343-361	1.0e-10	0.0	2.0e-13	3.4e-12
361-379	9.8e-11	0.0	1.5e-15	2.0e-13
379-397	9.3e-11	0.0	1.6e-17	4.3e-15
397-415	9.0e-11	0.0	1.4e-18	5.5e-16

^a Merger rate density of double compact objects within the horizon of advanced LIGO/Virgo obtained with three different methods: I, II, III for one underlying evolutionary model V2 (see Sec. 2 for details).

^b Our binning corresponds to the initial LIGO/Virgo low- and high-mass search bins, extended above 109 M_{\odot} with equal mass bins of 18 M_{\odot} .

^cExpected advanced LIGO/Virgo upper limits (Sec. 4.2).

TABLE 2
EVOLUTIONARY MODELS^a

Model	Name	Description
V1	optimistic	in CE: HG donors allowed
V2	standard	λ =physical, decreased BH kicks, rapid SN, HG CE donors not allowed
V3	pessimistic	full natal kicks for BHs
V4	no mass-gap	delayed supernova engine

^a For each model (V1–V4) we provide merger rate densities in low-metallicity (l: e.g., V1l) and high-metallicity (h: e.g., V2h) evolution scenarios.

TABLE 3
LOW-*Z* MERGER RATE DENSITY FOR iLIGO/VIRGO [MPC⁻³ YR⁻¹] ^a

$M_{\text{tot},z}/ M_{\odot}$ ^b	iLIGO ^c	Models			
		V1l	V2l	V3l	V4l
2–5	7.5e-05	1.3e-07	5.0e-08	5.1e-08	5.7e-08
5–8	2.5e-05	9.3e-10	5.2e-11	1.2e-12	7.8e-10
8–11	1.0e-05	1.6e-08	1.7e-09	2.9e-10	8.6e-10
11–14	7.5e-06	2.3e-08	2.8e-09	7.9e-11	1.2e-09
14–17	5.0e-06	9.8e-08	1.1e-08	1.2e-10	9.6e-10
17–20	3.8e-06	1.6e-08	1.6e-09	7.9e-12	1.2e-09
20–25	3.2e-06	2.4e-08	2.5e-09	6.4e-12	3.6e-09
25–37	8.7e-07	4.9e-08	1.3e-08	4.0e-11	1.1e-08
37–54	3.3e-07	7.9e-09	4.5e-09	1.4e-11	4.1e-09
54–73	1.7e-07	3.4e-09	6.0e-10	2.5e-12	4.9e-10
73–91	9.0e-08	8.5e-10	2.1e-10	7.2e-11	2.3e-10
91–109	7.0e-08	2.8e-11	1.6e-11	1.5e-11	9.2e-12
109–127	—	4.4e-12	3.4e-12	7.7e-14	1.2e-11
127–145	—	0.0	0.0	0.0	1.2e-15
145–163	—	0.0	0.0	0.0	0.0

^a Merger rate density of double compact objects calculated using full inspiral–merger–ringdown waveforms (method II). Rate densities are given for the low-metallicity evolution scenario.

^b Our binning corresponds to the initial LIGO/Virgo low- and high-mass search bins.

^c Available initial LIGO/Virgo upper limits for equal mass mergers.

TABLE 4
HIGH-Z MERGER RATE DENSITY FOR iLIGO/VIRGO [$\text{MPC}^{-3} \text{YR}^{-1}$] ^a

$M_{\text{tot},z}/M_{\odot}$ ^b	iLIGO ^c	Models			
		V1h	V2h	V3h	V4h
2–5	7.5e-05	1.6e-07	5.7e-08	5.8e-08	6.8e-08
5–8	2.5e-05	5.1e-10	2.0e-10	9.9e-13	3.6e-10
8–11	1.0e-05	1.4e-08	2.0e-09	3.4e-11	3.5e-10
11–14	7.5e-06	1.1e-08	2.5e-09	4.3e-11	6.1e-10
14–17	5.0e-06	6.5e-08	1.3e-08	1.8e-10	8.4e-10
17–20	3.8e-06	6.0e-09	7.3e-10	4.0e-11	6.8e-10
20–25	3.2e-06	9.2e-09	1.7e-09	8.9e-12	1.7e-09
25–37	8.7e-07	1.7e-08	7.0e-09	2.0e-11	8.0e-09
37–54	3.3e-07	3.2e-09	2.0e-09	6.8e-12	1.9e-09
54–73	1.7e-07	2.0e-09	4.3e-10	3.1e-12	3.1e-10
73–91	9.0e-08	5.8e-10	1.5e-10	5.4e-11	1.3e-10
91–109	7.0e-08	1.5e-11	1.5e-11	1.7e-11	1.2e-11
109–127	—	1.6e-12	1.6e-12	0.0	5.2e-12
127–145	—	0.0	0.0	0.0	6.9e-16
145–163	—	0.0	0.0	0.0	0.0

^a Merger rate density of double compact objects calculated using full inspiral–merger–ringdown waveforms (method II). Rate densities are given for the high-metallicity evolution scenario.

^b Our binning corresponds to the initial LIGO/Virgo low- and high-mass search bins.

^c Available initial LIGO/Virgo upper limits for equal mass mergers.

TABLE 5
 LOW- Z MERGER RATE DENSITY FOR ALIGO/VIRGO [$\text{MPC}^{-3} \text{YR}^{-1}$] ^a

$M_{\text{tot},z}/ M_{\odot}$ ^b	aLIGO ^c	Models			
		V11	V21	V31	V41
2–5	1.2e-07	1.5e-07	5.7e-08	5.4e-08	6.2e-08
5–8	3.3e-08	7.8e-10	3.0e-11	5.2e-13	8.3e-10
8–11	1.6e-08	1.5e-08	1.7e-09	6.0e-10	7.1e-10
11–14	1.0e-08	8.8e-09	1.2e-09	1.6e-10	9.7e-10
14–17	6.7e-09	7.0e-08	6.4e-09	8.2e-11	1.1e-09
17–20	4.9e-09	9.0e-08	8.9e-09	1.2e-10	1.0e-09
20–25	3.6e-09	4.3e-08	3.8e-09	6.3e-11	2.7e-09
25–37	2.2e-09	8.4e-08	1.1e-08	1.5e-10	1.3e-08
37–54	1.2e-09	7.4e-08	1.5e-08	1.0e-10	1.6e-08
54–73	7.7e-10	2.3e-08	4.9e-09	1.1e-10	4.9e-09
73–91	5.6e-10	6.2e-09	1.7e-09	9.9e-11	1.6e-09
91–109	4.3e-10	4.5e-09	4.5e-10	3.7e-11	4.9e-10
109–127	3.5e-10	2.5e-09	2.7e-10	1.7e-11	3.8e-10
127–145	2.9e-10	9.3e-10	2.1e-10	6.0e-12	2.5e-10
145–163	2.5e-10	2.7e-10	8.8e-11	5.0e-12	1.2e-10
163–181	2.2e-10	1.5e-10	7.8e-11	3.6e-12	9.9e-11
181–199	2.0e-10	1.1e-10	6.8e-11	9.3e-13	7.1e-11
199–217	1.8e-10	8.1e-11	4.7e-11	2.8e-12	4.5e-11
217–235	1.6e-10	5.4e-11	3.0e-11	4.9e-12	2.9e-11
235–253	1.5e-10	2.4e-11	7.9e-12	6.0e-12	1.8e-11
253–271	1.4e-10	1.0e-11	4.8e-12	3.0e-13	4.8e-12
271–289	1.3e-10	6.4e-12	4.3e-12	3.7e-14	9.9e-13
289–307	1.2e-10	2.8e-12	3.1e-12	4.3e-14	6.9e-13
307–325	1.1e-10	9.0e-13	1.0e-12	1.7e-14	4.9e-13
325–343	1.1e-10	1.0e-12	6.6e-13	4.0e-15	9.0e-13
343–361	1.0e-10	1.8e-13	2.0e-13	1.0e-18	4.6e-13
361–379	9.8e-11	1.8e-15	1.5e-15	0.0	9.7e-14
379–397	9.3e-11	1.2e-17	1.6e-17	0.0	1.3e-16
397–415	9.0e-11	1.9e-18	1.4e-18	0.0	8.2e-19

^a Merger rate density of double compact objects calculated with method II for advanced LIGO/Virgo. Rate densities are given for low-metallicity evolution scenario.

^b Our binning corresponds to the initial LIGO/Virgo low- and high-mass search bins extended to higher masses.

^cExpected advanced LIGO/Virgo upper limits (Sec. 4.2).

TABLE 6
HIGH-Z MERGER RATE DENSITY FOR ALIGO/VIRGO [$\text{MPC}^{-3} \text{YR}^{-1}$] ^a

$M_{\text{tot},z}/ M_{\odot}$ ^b	aLIGO ^c	V1h	Models		
			V2h	V3h	V4h
2–5	1.2e-07	1.7e-07	6.4e-08	5.9e-08	6.8e-08
5–8	3.3e-08	2.7e-10	4.5e-11	1.7e-13	4.6e-10
8–11	1.6e-08	1.3e-08	1.6e-09	6.4e-11	4.7e-10
11–14	1.0e-08	4.8e-09	6.9e-10	9.1e-11	5.4e-10
14–17	6.7e-09	4.4e-08	7.2e-09	6.9e-11	7.1e-10
17–20	4.9e-09	5.7e-08	1.1e-08	7.6e-11	7.8e-10
20–25	3.6e-09	2.0e-08	3.5e-09	3.5e-11	1.6e-09
25–37	2.2e-09	3.3e-08	6.5e-09	1.0e-10	7.5e-09
37–54	1.2e-09	2.9e-08	9.1e-09	6.0e-11	7.6e-09
54–73	7.7e-10	7.0e-09	2.2e-09	7.0e-11	2.2e-09
73–91	5.6e-10	2.9e-09	8.0e-10	6.7e-11	8.4e-10
91–109	4.3e-10	2.5e-09	2.8e-10	2.4e-11	3.3e-10
109–127	3.5e-10	1.4e-09	1.8e-10	1.1e-11	2.5e-10
127–145	2.9e-10	5.5e-10	1.5e-10	4.0e-12	1.8e-10
145–163	2.5e-10	1.6e-10	5.2e-11	2.2e-12	7.3e-11
163–181	2.2e-10	7.8e-11	4.4e-11	3.5e-12	7.1e-11
181–199	2.0e-10	6.0e-11	4.2e-11	2.8e-13	4.1e-11
199–217	1.8e-10	4.3e-11	2.7e-11	1.2e-12	2.8e-11
217–235	1.6e-10	3.4e-11	1.9e-11	2.5e-12	1.7e-11
235–253	1.5e-10	1.3e-11	5.1e-12	4.3e-12	1.2e-11
253–271	1.4e-10	5.8e-12	2.1e-12	3.6e-13	3.6e-12
271–289	1.3e-10	3.5e-12	2.9e-12	4.6e-15	4.1e-13
289–307	1.2e-10	1.7e-12	1.7e-12	1.3e-14	2.8e-13
307–325	1.1e-10	7.1e-13	5.6e-13	1.0e-14	2.5e-13
325–343	1.1e-10	4.5e-13	4.8e-13	3.8e-15	2.4e-13
343–361	1.0e-10	1.8e-13	1.9e-13	0.0	5.1e-13
361–379	9.8e-11	1.5e-14	4.1e-16	0.0	4.3e-14
379–397	9.3e-11	0.0	1.4e-18	0.0	1.8e-17
397–415	9.0e-11	0.0	0.0	0.0	0.0

^a Merger rate density of double compact objects calculated with method III for advanced LIGO/Virgo. Rate densities are given for the high-metallicity evolution scenario.

^b Our binning corresponds to the initial LIGO/Virgo low- and high-mass search bins extended to higher masses.

^c Expected advanced LIGO/Virgo upper limits (Sec. 4.2).

TABLE 7
BLACK HOLE MASS AND NATAL KICK ^a

No	Name	Mass [M_{\odot}]	Natal Kick [km s^{-1}]
1)	GRO J1655-40 (Nova Sco 94)	5.3 ± 0.3 (3,21)	0–210 (4)
2)	XTE J1118+480	7.6 ± 0.7 (10)	80–310 (11)
3)	GS 2023+338 (V404 Cyg)	$9.0^{+0.2}_{-0.6}$ (17)	0–45 (23,1) ^b
4)	GRS 1915+105	$12.4^{+2.0}_{-1.8}$ (13) ^c	0–75 (24,13,1)
5)	Cyg X-1	14.8 ± 1.0 (18)	0–60 (19,20)
6)	4U 1543-47	5.1 ± 2.4 (22)	> 80 (2), > 75 (1)
7)	H 1705-250 (Nova Oph 77)	6.4 ± 1.5 (5)	> 217 (6) ^d , > 0 (1)
8)	A 0620-00 (V616 Mon)	6.6 ± 0.25 (8)	> 20 (6), > 0 (1)
9)	GRS 1124-68 (Nova Mus 91)	7.0 ± 0.6 (9)	> 62 (6), > 0 (1)
10)	GS 2000+251	7.2 ± 1.7 (7)	> 24 (6), > 0 (1)
11)	GRS 1009-45 (Nova Vel 93)	8.5 ± 1.0 (12) ^e	> 49 (6), > 0 (1)
12)	XTE J1819-254 (V4641 Sgr)	10.2 ± 1.5 (14)	> 190 (2), > 100 (1)
13)	GRO J0422+32	> 10.4 (15)	> 35 (6), > 0 (1)
14)	XTE J1550-564	10.5 ± 1.0 (16)	> 10 (2), > 0 (1)

^a References for the mass and natal kick estimates are given in parentheses: (1) this study; see Sec. 6, (22) Orosz et al. (1998), (2) Repetto et al. 2012, (3) Motta et al. (2014), (4) Willems et al. (2005), (5) Harlaftis et al. (1997), (6) Repetto & Nelemans (2015), (7) Ioannou et al. (2004), (8) Cantrell et al. (2010), (9) Gelino et al. (2001), (10) Khargharia et al. (2013), (11) Fragos et al. (2009), (12) Macias et al. (2011), (13) Reid et al. (2014), (14) Orosz et al. (2001), (15) Reynolds et al. (2007), (16) Li et al. (2013), (17) Khargharia et al. (2010), (18) Orosz et al. (2011), (19) Mirabel & Rodrigues (2003), (20) Wong et al. (2012), (21) Beer & Podsiadlowski 2002, (23) Miller-Jones et al. 2009, (24) Dhawan et al. (2007).

^bThe quoted range refers to our own simple estimate based on 3D peculiar velocity presented in (23).

^cThere is also an alternative BH mass estimate of $12.9 \pm 2.4 M_{\odot}$ (Hurley et al. 2013). These observations were superseded with much higher resolution spectra and analysis of Steeghs et al. (2013) that resulted in a BH mass of $10.1 \pm 0.6 M_{\odot}$. Recently revised system parallax/distance led to further correction of the BH mass to the value included in this Table.

^dReported lower limit of 415 km s^{-1} (6) was revised later by the first author of (6) to 217 km s^{-1} . The revision is a result of a mistake made in calculation for just this one system in (6).

^eError estimate: Jerome Orosz 2014, priv. communication.

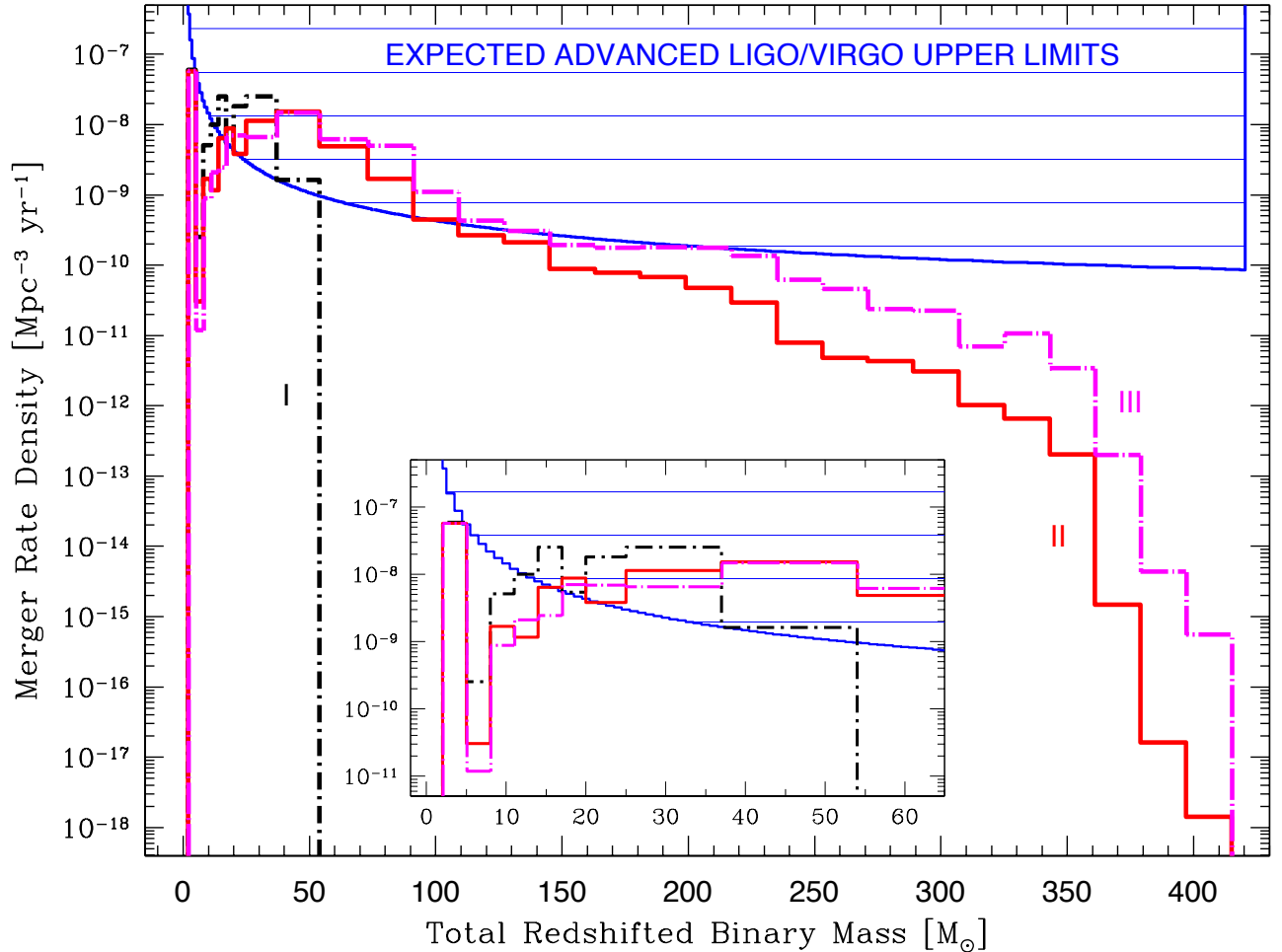


Fig. 1.— Comparison of methods for double compact object merger rate density estimate. The estimate is performed for advanced LIGO/Virgo. The rate density is subdivided into total merger mass bins. The predicted merger masses are redshifted to correspond to a detectable quantity. The theoretical predictions are shown for one underlying population synthesis evolutionary model (V21). The three lines demonstrate the sensitivity of the predictions to the adopted method of transferring population synthesis results into merger rate density: method I (black short dashed-dotted line), method II (red solid line), and method III (magenta long dashed-dotted line). The blue line shows expected advanced LIGO/Virgo upper limits. The inset zooms in on mergers with relatively low total mass. Method II gives the current best estimate of the merger rate density from population synthesis results to be directly compared with LIGO/Virgo upper limits. Redshifted total mass of potentially detectable binaries can reach $400 M_{\odot}$ (corresponding to a redshift $z = 2$ merger with a total intrinsic mass of $130 M_{\odot}$). Method III is an extension of method II as it gives merger rate density within entire (spherical) volume enclosed by a detector horizon redshift (and not only within a smaller “peanut” shaped volume sampled directly by a detector: method II). As expected, higher rate density of massive BH-BH mergers is found with this method. Method I fails dramatically at higher masses. Variants of this method are generally used within the population synthesis to generate rate predictions for double compact object merger rates. For example, all the detection probabilities/merger rates presented within Abadie et al. (2010) use Method I or even simpler approaches.

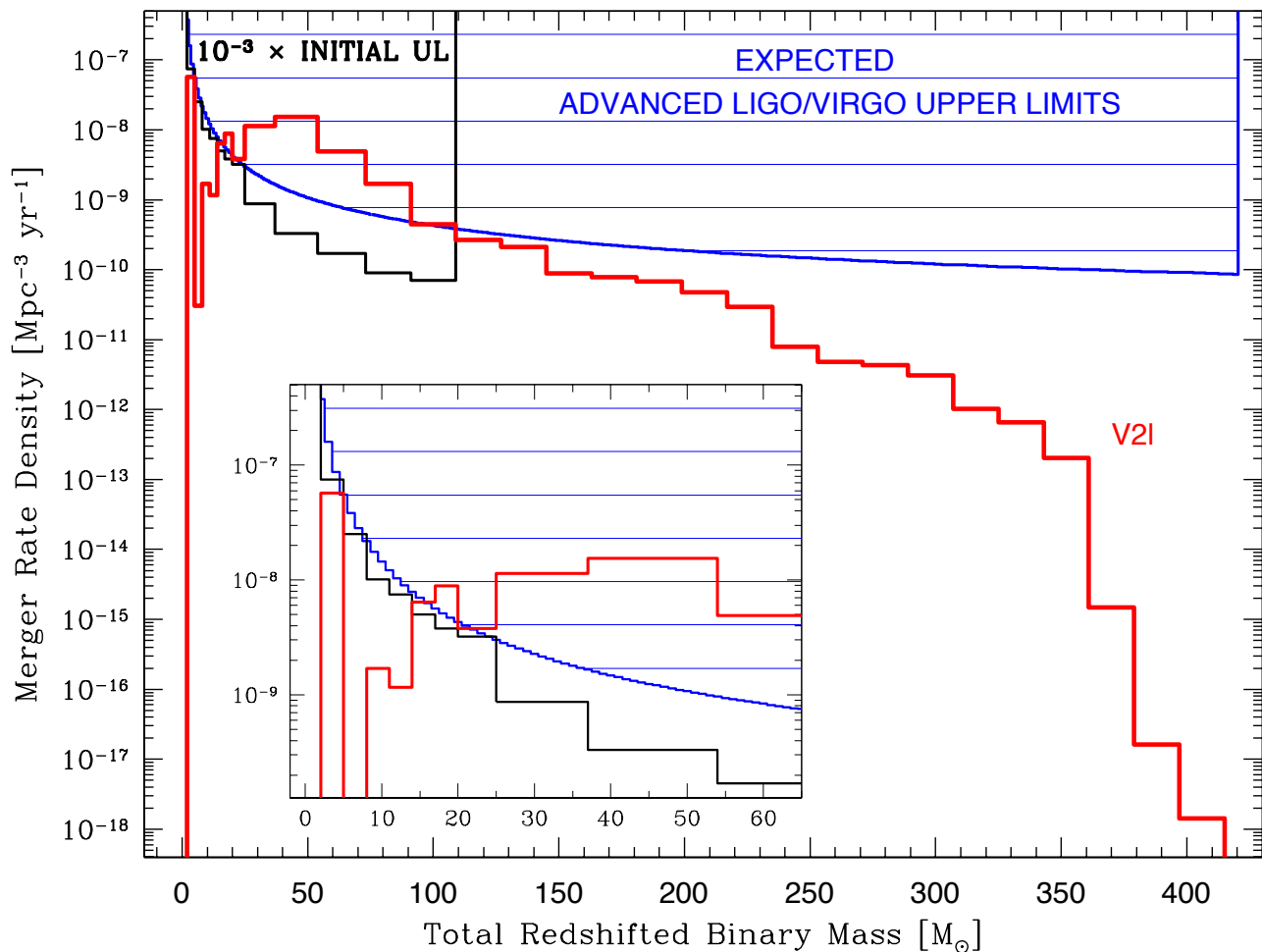


Fig. 2.— Comparison of detailed calculations of the expected advanced LIGO/Virgo upper limits on double compact object merger rate density (blue; thick solid line with shaded area) with the simple estimate (black; thin solid line). The detailed upper limits are obtained with full waveforms (inspiral–merger–ringdown) and with the advanced detector sensitivity curve (see Sec. 4.2). The simple estimate is calculated by multiplying the existing initial LIGO/Virgo upper limits by factor of 10^{-3} , which corresponds to a rough estimate of the difference in volume sampled by initial and advanced instruments. Note that above a total merger mass of $25 M_{\odot}$ the simple estimate breaks down (the upper limits are significantly too deep). For comparison we show our predicted merger rate density for our standard evolutionary model for low metallicity (V2I) and calculated with method II.

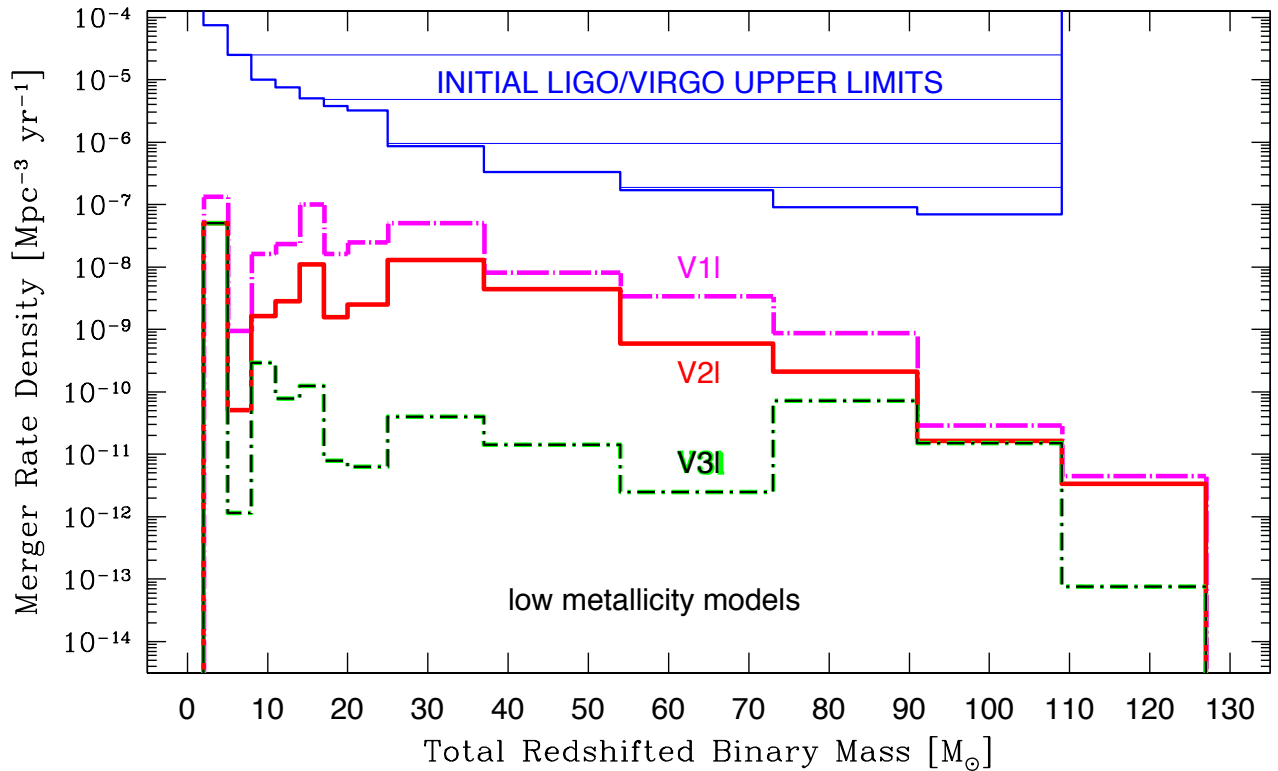


Fig. 3.— Merger rate density of double compact objects for our low metallicity evolution scenario predicted (with method II) for initial LIGO/Virgo. Note that the predictions are very close to the upper limits (within a factor of 18) for model V1 for total merger masses of 25–37 M_{\odot} . The merger rate density decreases from model V1 (optimistic CE), to V2 (standard binary evolution), to V3 (high BH natal kicks). Model V4 (not shown) results in a very similar merger rate density level to model V2, with the exception that the second mass bin (5–8 M_{\odot}) does not show a characteristic drop (mass gap) found in other models. The top shaded area shows the upper limits from initial LIGO/Virgo.

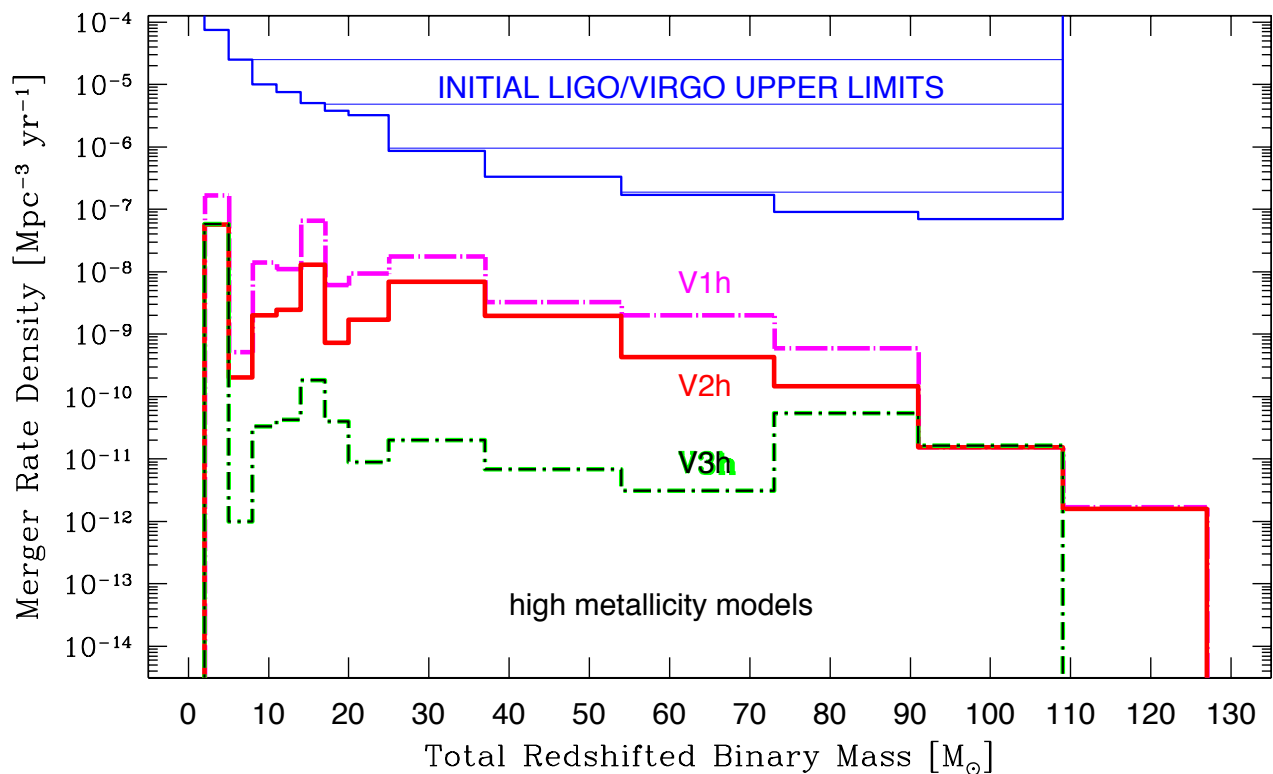


Fig. 4.— Merger rate density of double compact objects for our high metallicity evolution scenario predicted (with method II) for initial LIGO/Virgo. Otherwise the same as Fig. 3. Note that although the metallicity is a key factor in the formation of double compact object binaries, the variation of the cosmological metallicity evolution scenario does not significantly affect merger rate densities. For example, in model V2 the merger rate density decreases by less than a factor of ~ 4 in all mass bins when going from low to high metallicity evolutionary scenarios (see also Table 2 and Table 3).

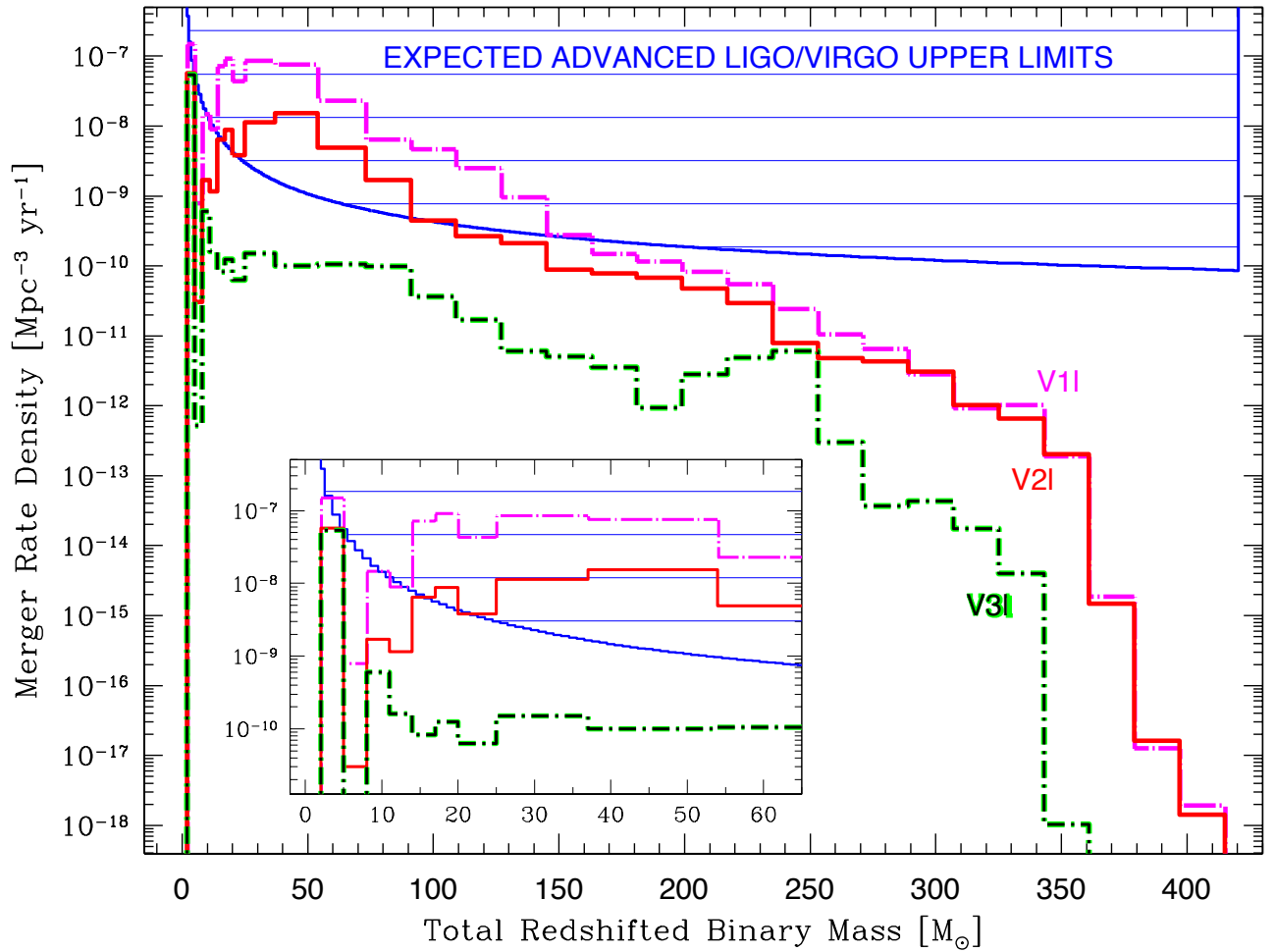


Fig. 5.— Merger rate density of double compact objects for our low metallicity evolution scenario predicted (with method II) for advanced LIGO/Virgo. Note that the predictions for our optimistic (V1I) and standard (V2I) models are above the projected upper limits, while for our pessimistic model (V3I) the predictions are below the upper limits. The most likely detections are predicted for BH-BH mergers with total redshifted mass 25–73 M_{\odot} (three highest mass bins above upper limits).

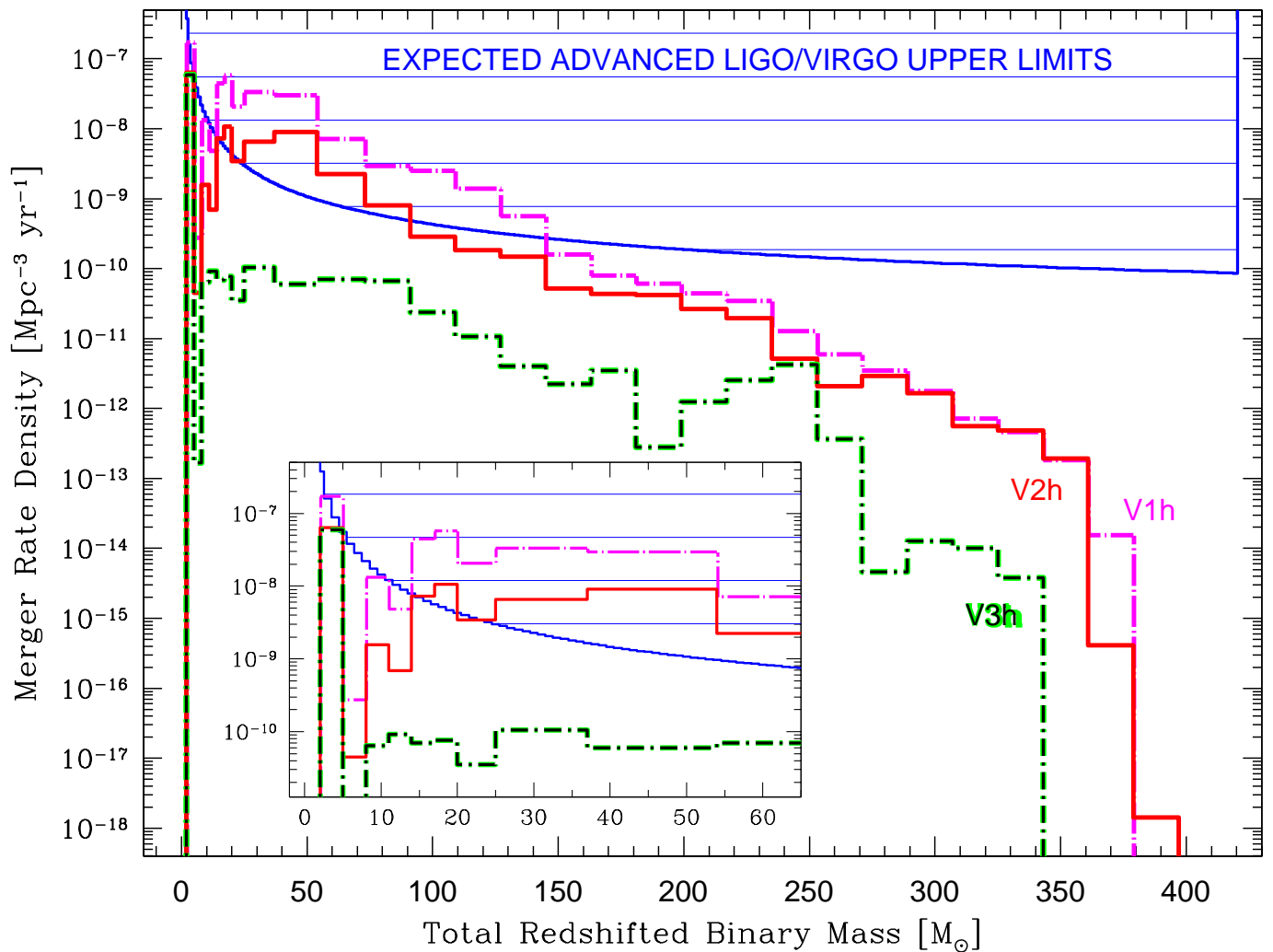


Fig. 6.— Merger rate density of double compact objects for our high metallicity evolution scenario predicted (with method II) for advanced LIGO/Virgo. Note that the predictions for our optimistic (V1h) and standard (V2h) models are above the projected upper limits, while for our pessimistic model (V3h) the predictions are below the upper limits. The most likely detections are predicted for BH-BH mergers with total redshifted mass 25–73 M_{\odot} (three highest mass bins above upper limits).

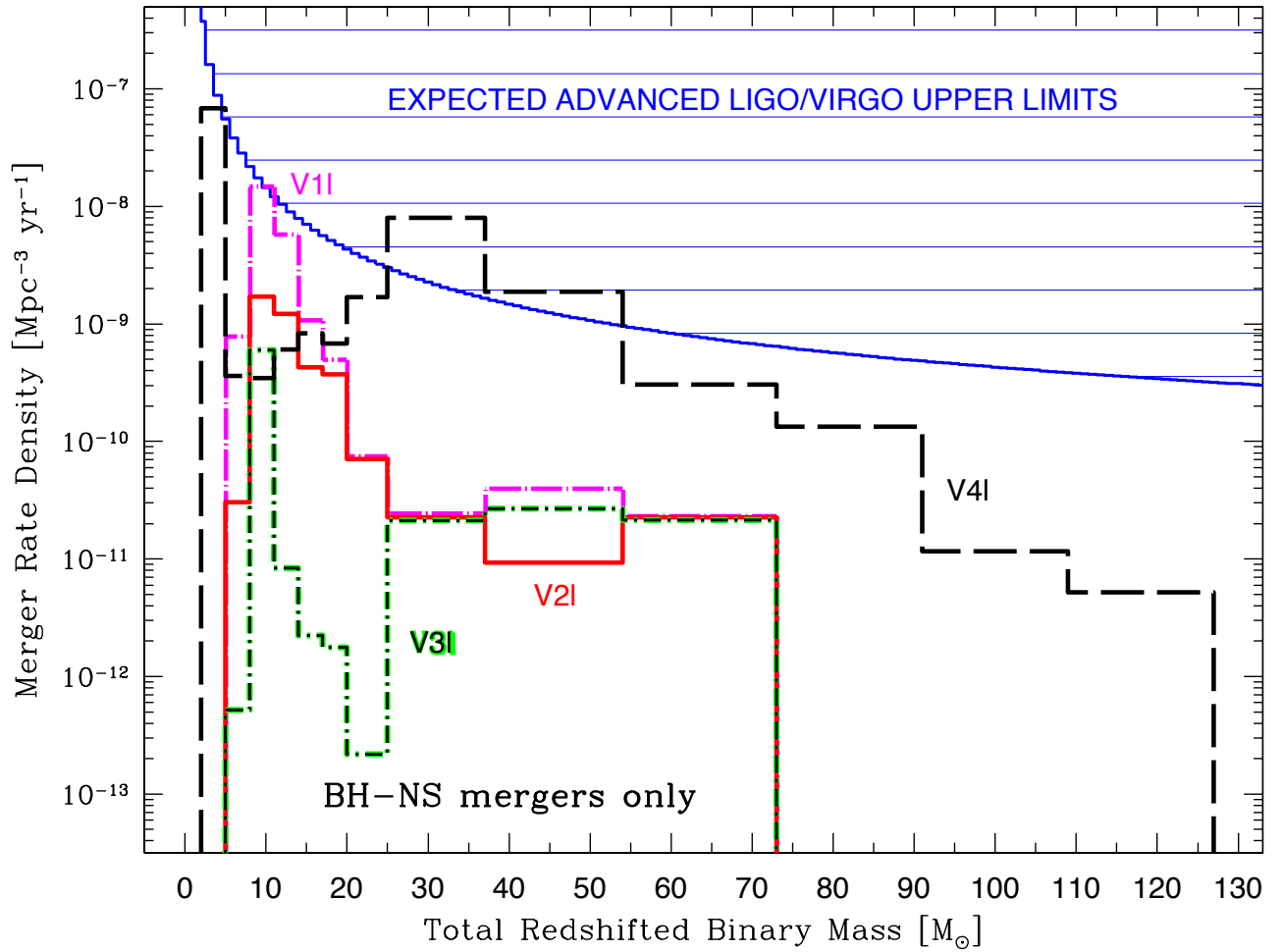


Fig. 7.— Merger rate density for BH-NS systems for our low metallicity evolution scenario predicted (with method II) for advanced LIGO/Virgo. Note that only the delayed SN explosion model (V4) and the optimistic model (V1) make detections likely, while the other models indicate non-detection even at the full advanced LIGO/Virgo sensitivity.

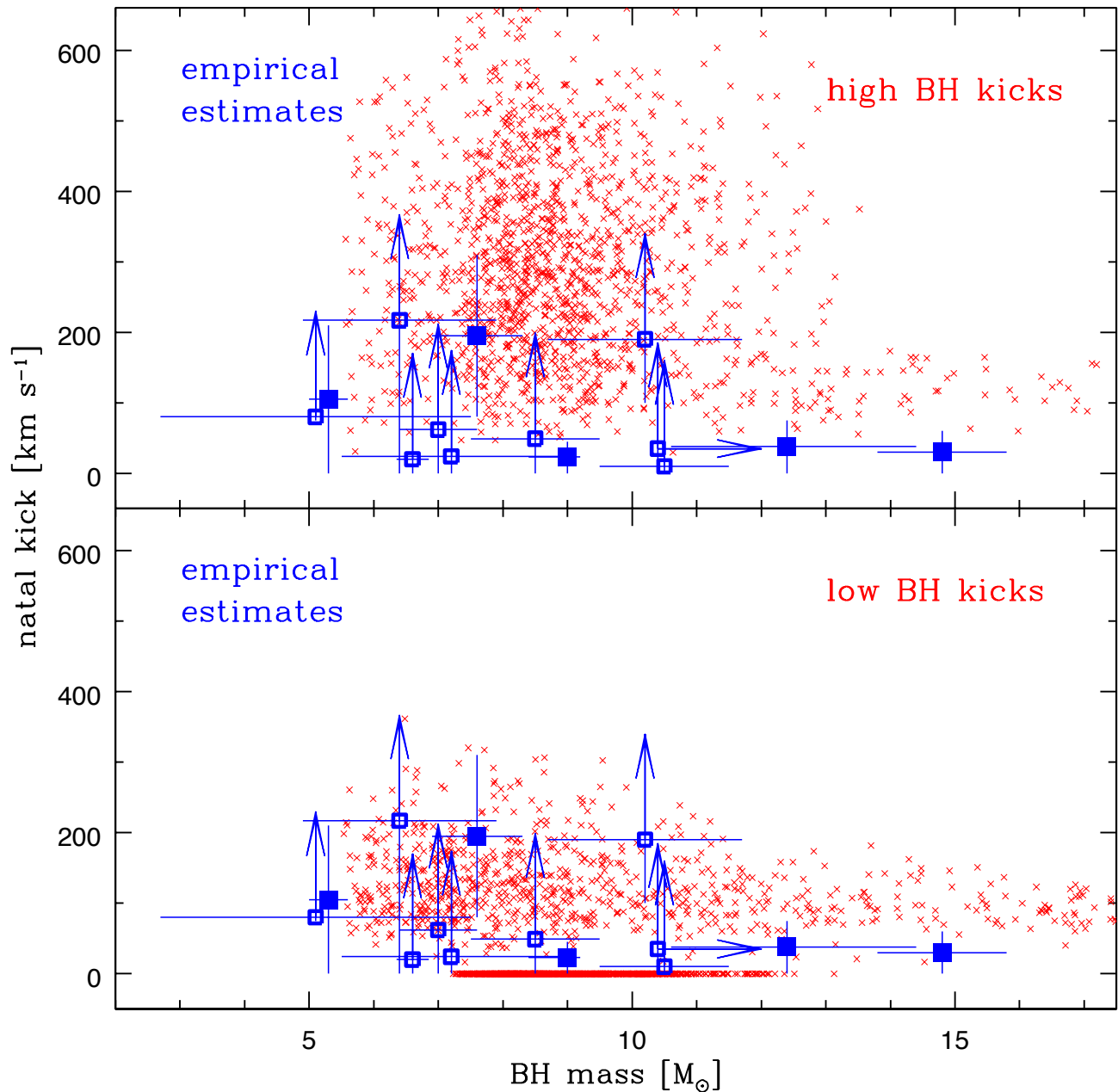


Fig. 8.— Black hole natal kick empirical estimates (blue; squares) for 14 Galactic X-ray binaries. Actual natal kick estimates based on 3D peculiar velocities are available for 5 binaries (filled squares). Lower limits based on Galactic position are available for 9 binaries (empty squares with up-arrows). We have re-evaluated some of these lower limits down (lines reaching from the original lower limit down to the revised limit). The most extreme case is H 1705-250 with an original lower limit of 217 km s^{-1} and a revised limit of 0 km s^{-1} . Errors on BH mass estimates are marked with horizontal lines. For one system (GRO J0422+32) there is only a lower limit on the BH mass ($> 10.4 M_{\odot}$), marked with a right-arrow. The empirical data used in this plot is given in Table 7 and described in Sec. 6. The empirical estimates are contrasted with evolutionary predictions (red; small crosses) of Galactic BH interacting binaries. In one evolutionary model we have assumed high BH kicks (top panel): all BHs receive natal kicks as measured for single Galactic pulsars (Maxwellian with $1D \sigma = 265 \text{ km s}^{-1}$: an average kick of 420 km s^{-1}). In another model (bottom panel) we have adopted low BH kicks (approximately decreasing with BH mass; rapid supernova explosion model of Fryer et al. 2012). Contrary to some expectations that natal kicks decrease with BH mass, we point out that both theoretical models: natal kicks independent of BH mass and kicks decreasing with BH mass, can explain the empirical data within their associated errors. On one hand this reflects the fact that the empirical data is still very poor (only 5 good estimates and many weak lower limits). On the other hand this demonstrates that even model with natal kicks decreasing with BH mass may deliver a wide range of BH natal kicks. For low-mass BHs low and high kicks are expected as we draw them from Maxwellian with high $\sigma \approx 265 \text{ km s}^{-1}$. For high mass BHs, low to zero kicks are expected if a BH forms with high mass ($\sigma \approx 0 \text{ km s}^{-1}$), and higher kicks are expected for a BH that has formed at low-to-intermediate mass ($\sigma \approx 0\text{--}260 \text{ km s}^{-1}$) and then increased its mass via accretion from its companion.